
Polarisation Measurements for Storage Ring Electric Dipole Moment Investigations

von

Achim Andres

Masterarbeit in Physik

vorgelegt der

Fakultät für Mathematik, Informatik und Naturwissenschaften

RWTH Aachen

angefertigt am

III. Physikalischen Institut B

vorgelegt im **Mai 2020**

Erstgutachter und Betreuer

Prof. Dr. Jörg Pretz
III. Physikalisches Institut B
RWTH Aachen University

Zweitgutachter

Prof. Dr. Achim Stahl
III. Physikalisches Institut B
RWTH Aachen University

Contents

1. Introduction	1
2. Theoretical Background	2
2.1. Baryon Asymmetry	2
2.2. Electric Dipole Moments (EDMs)	3
2.3. Experimental Methods in Storage Rings	4
2.3.1. Main Principle	4
2.3.2. Magnetic Storage Rings - RF Wien Filter Method	5
2.3.3. Electric and Combined Storage Rings	8
3. The Cooler Synchrotron COSY	9
3.1. The Facility	9
3.1.1. Source and Cyclotron	9
3.1.2. COSY	10
3.2. Polarisation Manipulation & Detection	11
3.2.1. RF Solenoid	11
3.2.2. RF Wien Filter	12
3.2.3. Phase & Frequency Feedback	12
3.2.4. WASA Detector	13
4. Data Analysis	15
4.1. Measurement Principle	15
4.2. Polarimetry	15
4.3. Vertical Polarisation	19
4.4. Mapping Method	21
4.4.1. Spin Phase Advance φ_s	21
4.4.2. True Amplitude & Phase	23
4.5. Fourier Method	26
4.5.1. Discrete Turn Fourier Transform	26
4.5.2. Amplitude & Phase	30
4.6. Spin Tune Determination	31
4.7. Comparison of the Methods	33
4.8. Mismatch of the Wien Filter	34
4.8.1. Unpolarised Cycles	37
4.8.2. A new Online Monitoring Luminosity Tool	38

4.8.3.	Cycles with Phase Feedback	40
4.8.4.	Cycles without Phase Feedback	46
4.9.	A Detailed Spectral Analysis with Artificial Neural Networks . .	50
4.9.1.	Neural Networks - An Introduction	50
4.9.2.	Generation of Data	54
4.9.3.	Network Training	54
4.9.4.	Results	59
5.	Conclusion	63
A.	Fourier Method - Calculations	65
A.1.	Fourier Parameters Error	65
A.2.	Fourier Amplitudes without luminosity effects	66
	Bibliography	68

1. Introduction

The **J**ülich **E**lectric **D**ipole moment **I**nvestigation (JEDI) collaboration at Forschungszentrum Jülich, Germany aims to directly measure the electric dipole moment of charged elementary particles like protons and deuterons for the first time. A statistical sensitivity of $\mathcal{O}(10^{-24})$ e-cm is expected in a first stage with the existing **C**ooler **S**ynchrotron storage ring COSY. Afterwards a new dedicated all-electric storage ring should increase the sensitivity. A nonzero electric dipole moment would be a new source of \mathcal{CP} violation if the \mathcal{CPT} theorem holds. In a first stage, the electric dipole moment is measured by its interaction with an electric field inside a novel RF Wien Filter device, which leads to a tiny vertical polarisation buildup of the initially horizontally polarised beam. In order to reach the desired sensitivity, systematic effects, which cause fake EDM signals, need to be reduced to their absolute minimum. In this thesis, a new source of a systematic effect, which fakes an EDM signal is discussed. It was found that a misaligned electromagnetic field inside the RF Wien Filter leads to periodic beam oscillations, which simultaneously change the luminosity in the detector. A new luminosity monitoring system is added to the DAQ (**D**ata **A**c**Q**uisition) system to monitor the movement of the beam, which can be used to adjust the electromagnetic field inside the RF Wien Filter to ensure stable working conditions and reduce systematic errors during the next precursor run of the EDM project.

This work is divided into five parts, this introduction being the first of it. Chapter 2 presents the theoretical background of this work, including the theory of the electric dipole moment (EDM) and the staged approach of the JEDI collaboration to measure the EDM. In chapter 3, a short introduction into the accelerator facility COSY, along with its main components, which are relevant for this work, is shown. The analysis of data taken during the first precursor run in November 2018, showing the periodic beam movement, is presented in chapter 4. Finally, a conclusions is given in the final chapter 5.

2. Theoretical Background

2.1. Baryon Asymmetry

Our whole world is made out of ordinary baryonic matter, which is still a great mystery in physics. Neither the Standard Model (SM) of elementary Particle Physics nor the theory of general relativity can explain the origin of matter. According to current theories, the big bang should have produced the same amount of both matter and antimatter. The Baryogenesis describes the process in the early universe when particles and their antiparticles annihilated, with only a small amount of matter surviving. This effect can be quantified by the ratio of the difference between the number of baryons n_B and antibaryons $n_{\bar{B}}$ and the number of photons n_γ , which are the main end products of annihilation processes. The ratio is called baryon to photon ratio η

$$\eta = \frac{n_B - n_{\bar{B}}}{n_\gamma} \approx \frac{1}{2} \frac{n_B - n_{\bar{B}}}{n_B + n_{\bar{B}}}. \quad (2.1)$$

This ratio can be determined independently from the power spectrum of temperature fluctuations in the Cosmic Microwave Background (CMB) and the abundances of light elements in the intergalactic medium (IGM). Both methods consistently give values of $\eta \propto 10^{-10}$ [1] while the standard model of elementary particle physics combined with the standard model of cosmology predicts a value of $\eta \propto 10^{-18}$ [2].

To explain the asymmetry between matter and antimatter, Andrei Sakharov identified three conditions in 1967, that have to be fulfilled [3]:

- 1) Baryon number B conservation violation, to explain the excess of baryon over antibaryon production, as in the initial state $B = 0$.
- 2) \mathcal{C} symmetry violation and \mathcal{CP} symmetry violation. If \mathcal{C} and \mathcal{CP} symmetries are fully conserved, interactions which produce more baryons than anti-baryons will not be counterbalanced by interactions which produce more anti-baryons than baryons.
- 3) Deviations from the thermal equilibrium as \mathcal{CPT} symmetry assures otherwise the compensation of processes increasing and decreasing the baryon number.

In recent observations, \mathcal{CP} violation has been found in many sources like Kaon [4] and B-Meson decays [5]. However, the amount of measured \mathcal{CP} invariance is too small to explain the observed baryon asymmetry. New sources of \mathcal{CP} violation are needed, such as the so-called electric dipole moment (EDM).

2.2. Electric Dipole Moments (EDMs)

Classically, the electric dipole moment (EDM) is a vectorial property and defined as

$$\vec{d} = \int_V \rho(\vec{r}) \cdot \vec{r} d^3r, \quad (2.2)$$

where ρ denotes the charge density. In elementary particle physics, it is a fundamental property of a particle. It is aligned parallel or antiparallel to the spin of a particle, since the quantization axis is the only distinguished direction in a particle. The electric dipole moment is defined as [6]

$$\vec{d} = d \cdot \vec{s} \quad \text{with} \quad d = \eta \frac{q\hbar}{2mc}, \quad (2.3)$$

where q and m are the particle's charge and mass respectively, \hbar is the reduced planck constant, c the speed of light and η^1 is a dimensionless quantity, denoting the strength of the electric dipole moment. The electric dipole moment is defined in analogy to the well known magnetic dipole moment (MDM) of a particle

$$\vec{\mu} = \mu \cdot \vec{s} \quad \text{with} \quad \mu = g \frac{q\hbar}{2mc}, \quad (2.4)$$

with the dimensionless g -factor. The hamiltonian of a particle at rest with a magnetic and electric dipole moment in external magnetic \vec{B} and electric \vec{E} fields is given by

$$\hat{\mathcal{H}} = -d \cdot \vec{s} \cdot \vec{E} - \mu \cdot \vec{s} \cdot \vec{B}. \quad (2.5)$$

Applying the parity operator \mathcal{P} and the time reversal symmetry operator \mathcal{T} leads to

$$\mathcal{P}(\hat{\mathcal{H}}) = +d \cdot \vec{s} \cdot \vec{E} - \mu \cdot \vec{s} \cdot \vec{B}, \quad (2.6)$$

$$\mathcal{T}(\hat{\mathcal{H}}) = +d \cdot \vec{s} \cdot \vec{E} - \mu \cdot \vec{s} \cdot \vec{B}. \quad (2.7)$$

Parity transformation (eq. 2.6) changes the sign of the electric field \vec{E} , but doesn't affect the spin \vec{s} and the orientation of the magnetic field \vec{B} , *i.e.*, the sign of the electric dipole moment term changes (violates \mathcal{P} invariance), while the magnetic dipole moment term remains negative (conserves \mathcal{P} invariance).

¹Don't confound the strength of the EDM η with the baryon asymmetry in eq. 2.1.

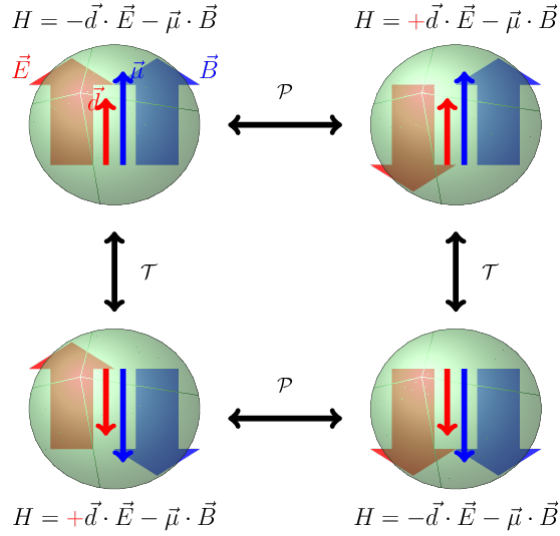


Figure 2.1.: Schematic drawing of a particle with a magnetic and electric dipole moment in an external magnetic and electric field. Under parity transformation, the electric field changes the sign. Under time reversal, the spin and the magnetic field change their signs, which leads to a different final state of the hamilonian for each operation [7].

In eq. 2.7, the spin \vec{s} and the magnetic field \vec{B} change the sign, which leads to the same conclusion as in eq. 2.6. Assuming that \mathcal{CPT} symmetry holds, a permanent, nonvanishing electric dipole moment for particles would mean a further source of \mathcal{CP} -violation. The breach of parity and time reversal symmetry can be seen in Figure 2.1.

2.3. Experimental Methods in Storage Rings

In this section, the methods of measuring the electric dipole moment of protons and deuterons are presented. In section 2.3.2 the method of the first ever direct measurement (also referred to as the precursor experiment) of the electric dipole moment with the existing storage ring COSY is described. In the following chapter, future experiments are explained which require new dedicated storage rings.

2.3.1. Main Principle

The basic principle of measuring an EDM is based on its interaction with external electric fields. An electric field \vec{E} in the rest frame of the particle tilts

the electric dipole moment \vec{d} . As the EDM is aligned parallel or antiparallel with the spin axis, the interaction leads to a buildup of the spin axis

$$\frac{d\vec{s}}{dt} \propto \vec{d} \times \vec{E}. \quad (2.8)$$

This tilt is used by all proposed storage rings to measure the EDM. The polarisation vector is initially in the horizontal plane. Therefore, the EDM rotates the spin vector vertically up- or downwards. The evolution of the spin vector under electromagnetic fields, including a non vanishing electric dipole moment component, is described by the Thomas - BMT equation. Assuming that the particle motion \vec{v} is perpendicular to the electric and magnetic field² [8]

$$\begin{aligned} \frac{d\vec{s}}{dt} &= \vec{s} \times \left(\vec{\Omega}^{\text{MDM}} + \vec{\Omega}^{\text{EDM}} \right) \quad \text{with} \quad (2.9) \\ \vec{\Omega}^{\text{MDM}} &= \frac{e\hbar}{mc} \left[G\vec{B} + \left(G - \frac{1}{\gamma^2 - 1} \right) c\vec{E} \times \vec{\beta} \right], \\ \vec{\Omega}^{\text{EDM}} &= \frac{e\hbar}{mc} \left[\frac{1}{2}\eta \left(\vec{E} + c\vec{\beta} \times \vec{B} \right) \right]. \end{aligned}$$

In eq. 2.9, $\vec{\Omega}^{\text{MDM}}$ and $\vec{\Omega}^{\text{EDM}}$ denote the angular velocities associated with the magnetic (MDM) and the electric dipole moment (EDM). \vec{E} and \vec{B} are external electric and magnetic fields in the laboratory frame, $G = (g - 2)/2$ is the anomalous g -factor and η is introduced in eq. 2.3. The Lorentz factors γ and $\vec{\beta}$ are used to describe the relativistic velocity of particles. $\vec{\beta}$ is defined as the ratio of the particles velocity \vec{v} and the speed of light in vacuum $\vec{\beta} = \vec{v}/c_0$. Using $\vec{\beta}$, γ can be calculated via $\gamma = 1/\sqrt{1 - |\beta|^2}$.

For an EDM measurement, the parameters in eq. 2.9 have to be chosen in such a way, that a macroscopic polarisation buildup can be measured.

2.3.2. Magnetic Storage Rings - RF Wien Filter Method

For a magnetic ring like COSY³, eq. 2.9 reduces to

$$\vec{\Omega}^{\text{MDM}} + \vec{\Omega}^{\text{EDM}} = \frac{e\hbar}{mc} \left[G\vec{B} + \frac{1}{2}\eta c\vec{\beta} \times \vec{B} \right], \quad (2.10)$$

where \vec{B} is the main magnetic field, oriented vertically, to bend the beam around the ring.

² $\vec{v} \cdot \vec{E} = \vec{0}$ and $\vec{v} \cdot \vec{B} = \vec{0}$.

³ $\vec{E} = \vec{0}$.

- **Vanishing EDM component ($\eta = 0$):** In this case, the spin precession is mainly driven by the magnetic field of the ring. The spin vector \vec{s} precesses around the vertical axis with a constant vertical component. The so-called spin tune can be defined as the ratio of the spin precession frequency and the revolution frequency,⁴

$$\nu_s = \frac{f_{\text{spin}}}{f_{\text{beam}}}, \quad (2.11)$$

and is given in the case of an ideal ring by

$$\nu_s = \gamma G, \quad (2.12)$$

which can be derived by plugging eq. 2.10 in eq. 2.9. Typical values for COSY are listed in table 2.1. Note that a negative spin tune means a counterclockwise spin rotation if the beam rotates clockwise. In an unperturbed ideal ring, the spins point 50% parallel to the particle motion and 50% antiparallel.

- **Non Vanishing EDM component ($\eta \neq 0$):** In the case of a non vanishing EDM component in eq. 2.10, $\vec{\Omega}^{\text{EDM}}$ will be inclined by a small angle and the spin vector \vec{s} will not only precess around the vertical axis. It gets an additional oscillating vertical component, as shown in Figure 2.2 (blue curve). However, the amplitude of the oscillation is too small to be detected directly and the net signal is zero. This is where the so-called RF Wien Filter enters the field.

A customary Wien Filter has an electrical \vec{E}_{WF} and a magnetic \vec{B}_{WF} field, perpendicular to each other and the beam direction. The total force on the beam must be zero at the desired momentum. If the particles are off-momentum, they are deflected either by the magnetic or electric field, hence the name filter. The RF Wien Filter was designed and built at the ZEA⁵ institute [9]. The RF Wien Filter works at the resonant frequency with the spin tune frequency

$$f_{\text{WF}} = f_{\text{rev}} |\gamma G \pm k| \text{ with } k \in \mathbb{Z}, \quad (2.13)$$

where f_{rev} denotes the revolution frequency of the beam. Every turn, the magnetic field of the RF Wien Filter \vec{B}_{WF} gives a small kick to the spin vector, which breaks the symmetry between parallel and antiparallel spin and particle

⁴The unit is given by spin precessions / turn in the accelerator.

⁵Zentralinstitut für Engineering, Elektronik und Analytik.

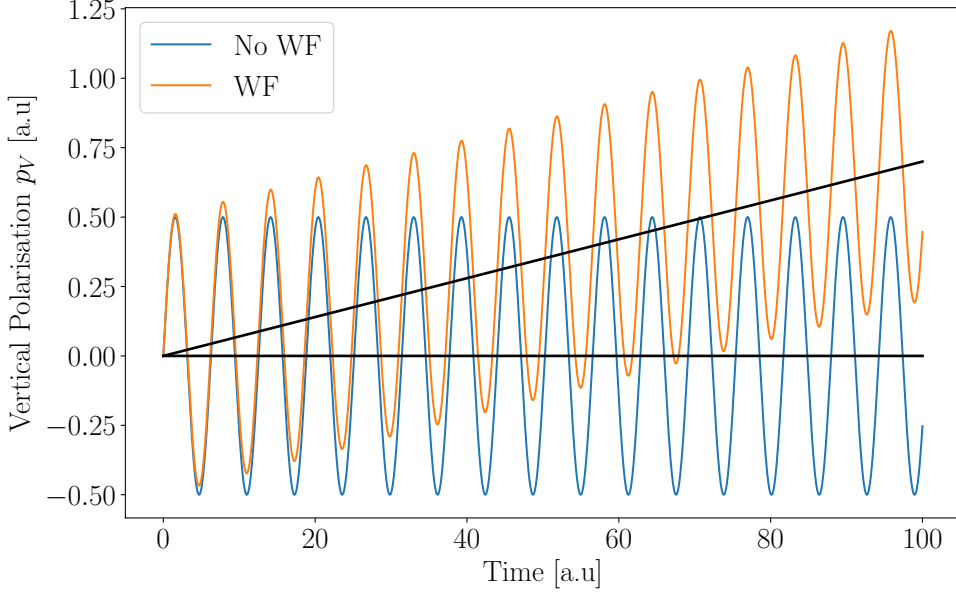


Figure 2.2.: Vertical polarisation buildup with and without Wien Filter (WF) in the ring with the measured signals in black.

motion. It can be shown, that the vertical polarisation build up is given by

$$\left(\frac{dP_V}{dt}\right)_{\text{EDM}} = \eta \frac{e\vec{B}_{\text{Wien}}}{4mc} \frac{1+G}{\gamma^2} P_0 \frac{e(-\vec{E}_R + \beta\vec{B}_V)}{mcv_s\omega_C}, \quad (2.14)$$

where \vec{E}_R denotes the radial electric field ($\vec{0}$ for COSY) and \vec{B}_V the vertical magnetic field [10]. The calculations assume that the phase difference between the spin tune precession and the RF Wien Filter is zero. Therefore a phase feedback system is necessary (see section 3.2.3) [11].

Table 2.1.: Rough estimates of particular values of deuterons (d) and protons (p) at a momentum of 970 MeV/c and 520 MeV/c in COSY respectively, including the particles revolution frequency f_{rev} , anomalous G factors [12, 13], Lorentz factors β and γ , the spin tune γG and the spin tune in units of hertz $f_{\text{prec}} = \gamma|G|f_{\text{rev}}$.

	$f_{\text{rev}}[\text{kHz}]$	G	β	γ	γG	$f_{\text{prec}}[\text{kHz}]$
d	750.2	-0.143	0.459	1.126	-0.161	120.1
p	791.6	1.793	0.458	1.143	2.050	1622.7

2.3.3. Electric and Combined Storage Rings

In a storage ring, using only electric bending components, eq. 2.9 reduces to

$$\vec{\Omega}^{\text{MDM}} + \vec{\Omega}^{\text{EDM}} = \frac{e\hbar}{mc} \left[\left(G - \frac{1}{\gamma^2 - 1} \right) c\vec{E} \times \vec{v} + \frac{1}{2}\eta\vec{E} \right] \quad (2.15)$$

It is of particular interest to reduce the angular velocity due to the MDM to zero ("frozen spin"). The condition

$$G - \frac{1}{\gamma^2 - 1} \stackrel{!}{=} 0 \quad (2.16)$$

is satisfied, if $p_{\text{magic}} = m_p/G = 0.7 \text{ GeV}$ holds. Note that this is only possible for protons, as $G_{\text{proton}} > 0$ [14].

A ring, using both electric and magnetic bending elements has to fulfill the following condition to reduce the MDM component to zero

$$G\vec{B} + \left(G - \frac{1}{\gamma^2 - 1} \right) c\vec{E} \times \vec{v} \stackrel{!}{=} \vec{0}. \quad (2.17)$$

This is possible for any charged particle. Such a ring design is being studied by the JEDI collaboration in Jülich [15].

3. The Cooler Synchrotron COSY

In this chapter an overview of the accelerator facility **CO**oler **SY**nchrotron **COSY** located at Forschungszentrum Jülich in Germany along with its main components relevant for this thesis is presented.

3.1. The Facility

The facility consists of three main parts: A source that provides polarised and unpolarised hydrogen H^- and deuterium D^- ion beams, a pre-accelerator cyclotron called JULIC (**JU**elich **L**ight **I**on **C**yclotron) and the main accelerator COSY. In Figure 3.1, a schematic of COSY is presented. COSY provides four internal and three external experimental sites, where hadron experiments can be carried out.

Once the particles are produced in the source and transported via the source beamline to the inner part of the cyclotron, the particles are accelerated and transferred via the injection beamline (IBL) to the synchrotron.

3.1.1. Source and Cyclotron

In total three ion sources are available: two for unpolarised (named after the companies IBA (Belgium) and AEA (Great Britain)) and one for polarised ion beams, providing hydrogen and deuterium ions with an energy of 4.5 keV and 7.6 keV, respectively. The polarisation process takes place during the collision of ground state nuclear polarised hydrogen or deuterium with an intense neutralized cesium beam



The polarised deuterium or hydrogen beam is afterwards extracted with a dipole magnet to the pre-accelerator JULIC [16]. The pre-accelerator cyclotron JULIC accelerates the unpolarised or polarised hydrogen H^- and deuterium D^- ion beams from the source up to their injection energies (45 MeV and 76 MeV for H^- and D^- beams respectively [17]). The cyclotron was built in 1968 and is used since 1992 as a pre-accelerator for COSY. It is an isochronous cyclotron,

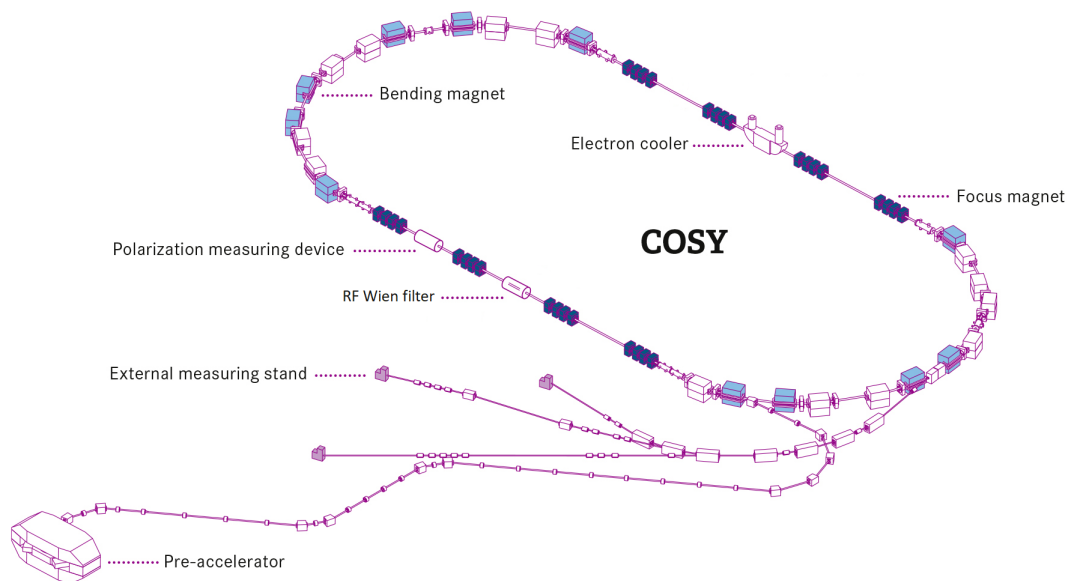


Figure 3.1.: Schematic overview of the facility. Starting at the pre-accelerator cyclotron JULIC, the ion beam is transferred to the main ring via the injection beamline. Included is an electron cooler, the RF Wien Filter and a polarisation measurement device [7].

separated in different sectors. The magnetic field inside the cyclotron increases with increasing radius to deliver constant relativistic beams. The different sectors guaranty horizontally focused ion beams.

From the cyclotron, the ions are transferred via the 94 m long injection beamline to COSY. On the injection beamline, a small polarimeter called LEP (**L**ow **E**nergy **P**olarimeter) is installed to measure the initial polarisation of the beam provided by the cyclotron [18]. At the end of the injection beamline, two electrons are removed from the ions by a thin carbon foil and the proton/deuteron beam is injected into COSY [19].

3.1.2. COSY

COSY is a synchrotron, accelerating deuteron and proton beams up to a momentum of $p = 3.7 \text{ GeV}/c$, which corresponds approximately to a kinetic energy of $E_{\text{kin},d} = 2.2 \text{ GeV}/c$ for deuterons and $E_{\text{kin},p} = 2.8 \text{ GeV}/c$ for protons [19].

The structure of the accelerator consists of two straight lines (40 m/line) and two arcs (52 m/arc), making it a so-called race track shaped ring. The total circumference is 184 m [19]. In the arcs, 24 normal conducting water cooled dipole magnets with a maximum magnetic field of 1.58 T bend the beam around

the ring. Furthermore, 56 quadrupole magnets focus the beam and sextupole magnets correct chromaticity effects, *i.e.* they minimize the beam dispersion. [20].

Besides the ability to accelerate polarised and unpolarised ion beams, COSY provides excellent beam conditions by cooling the beam using two electron coolers and a stochastic cooler, which reduce the emittance of the beam significantly.

Electron Cooling

Two electron coolers are installed in COSY, each in every straight section. In an electron cooler, electrons are accelerated with the same mean longitudinal velocity, but a smaller transverse velocity momentum spread than the main ion beam and guided via magnets into a short joint section with the main accelerator where the electrons interact with the ion beam. Due to the Coulomb interaction of oppositely charged particles, the momentum spread of the ion beam is reduced. After interacting with the beam, the electrons are guided via magnets out of the beam pipe [21].

Stochastic Cooling

COSY has a stochastic cooler, which consists of a pickup detector as well as a kicker. At the position of the pickup, the deviation of the particle beam from the design orbit is measured and the information is transferred diagonally from the pickup detector to the kicker. When the beam enters the kicker, a bump is applied to the beam, which corrects the deviation, allowing phase space reduction in the horizontal and longitudinal plane [21].

3.2. Polarisation Manipulation & Detection

In addition, several devices are installed in the ring to manipulate and detect the polarisation of the bunched beam, making COSY an ideal machine to study systematic effects on the road to a final electric dipole moment experiment. Some of these devices that are significant for this work, are presented in the following.

3.2.1. RF Solenoid

The RF solenoid used in COSY to rotate the initially vertical polarised beam longitudinally into the horizontal plane is a siberian snake. A siberian snake is used in polarised particle accelerators to avoid resonant spin tune crossings,

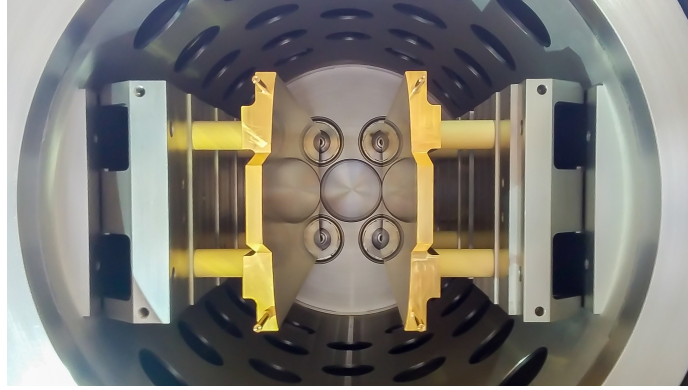


Figure 3.2.: Interior of the RF Wien Filter seen along the beam axis with two electrodes which produce the electromagnetic radio frequency field [7].

which cause depolarisation of the beam. The siberian snake in COSY is a 4.7 Tm longitudinally solenoid of 1 m length [22].

3.2.2. RF Wien Filter

A conventional Wien filter has orthogonal static electric and magnetic fields, used to filter off momentum particles. The particles are either deflected by the electric or the magnetic field. The particle beam must enter the Wien Filter in the center, where the Lorentz force \vec{F}_L is zero for particles with nominal velocity. This ensures that no beam oscillations are excited, which makes it an ideal device to manipulate spins of polarised particles. The purpose of the RF Wien Filter is to rotate the beam polarisation horizontally to break the symmetry between parallel and antiparallel spin and beam motion to accumulate a measurable EDM signal (see chapter 2.3.2). The interior with two electrodes of the RF Wien Filter can be seen in Figure 3.2 [23].

3.2.3. Phase & Frequency Feedback

To determine the precession of the EDM with an RF Wien Filter, not only its operation on a harmonic of the horizontal spin precession has to be guaranteed. Additionally, the relative phase of the precession rate and the RF device needs to be fixed. The phase difference of spin precession and rf frequency is defined as

$$\phi(t) = 2\pi (t - t_0) \cdot (f_{\text{rf}} - \nu_s f_{\text{cosy}}) + \phi_0, \quad (3.2)$$

where ϕ_0 is the phase at the time of starting the measurement $t = t_0$. Using $n/f_{\text{cosy}} = t - t_0$, where n denotes the turn number, eq. 3.2 reduces to

$$\phi(n) = 2\pi n \left(\frac{f_{\text{rf}}}{f_{\text{cosy}}} - \nu_s \right) + \phi_0. \quad (3.3)$$

As long as the Wien Filter condition (eq. 2.13) is fulfilled, $\phi(n)$ stays constant. However, even small mismatches between the rf frequency f_{rf} and the resonance frequency lead to continuous changes of $\phi(n)$. The basic principle of the feedback is to control the phase by adjusting the frequency of the cavity f_{cosy} . It can be shown that the necessary frequency change Δf_{cosy} is given by [11]

$$\Delta\phi \approx 6.93 \frac{\text{rad}}{\text{Hz s}} \Delta f_{\text{cosy}} \Delta t. \quad (3.4)$$

3.2.4. WASA Detector

The WASA (**W**ide **A**ngle **S**hower **A**pparatus) was built in 1996 at the Department of Radiation Sciences at the University Uppsala and installed at the storage ring CELSIUS. In 2006, the entire detector was moved to COSY for the Wasa at COSY collaboration. It consisted of two main parts: a central part and a forward part. After taking data for eight years, the physics program of WASA ended and the central part was removed from the detector. Nowadays, the forward part is used as a polarimeter for the EDM project [24]. The detector consists of multiple pizza-shaped layers, that work as triggers and detectors for penetrating particles after they scatter with the unpolarised internal target. For the purpose of a polarimeter, the detector is subdivided into four sections, each covering an azimuthal angle of $\Delta\Phi \approx 90^\circ$. The four detectors are called up, down, left and right, as seen from the beam direction. A sketch of the detector with its layers is shown in Figure 3.3. The angular coverage is $\Theta = 2^\circ - 17^\circ$ and $\Phi = 0^\circ - 360^\circ$. A coordinate system defining the angles is shown in Figure 4.2. The extraction on the target is provided by a white noise electric field, which consists of superimposed sinusoidal signals. The extraction rate on the target is controlled by a feedback system called Schneider Box. It controls the voltage of the white noise applied to the beam so that the extraction rate stays constant with time.

In November 2019, a new dedicated polarimeter called JePo (**J**edi **P**olarimeter) based on LYSO crystals was installed in the ring, to increase the sensitivity of measuring the polarisation build-up due to the EDM [26]. A picture of JePo is shown in Figure 3.4.

3.2. POLARISATION MANIPULATION & DETECTION

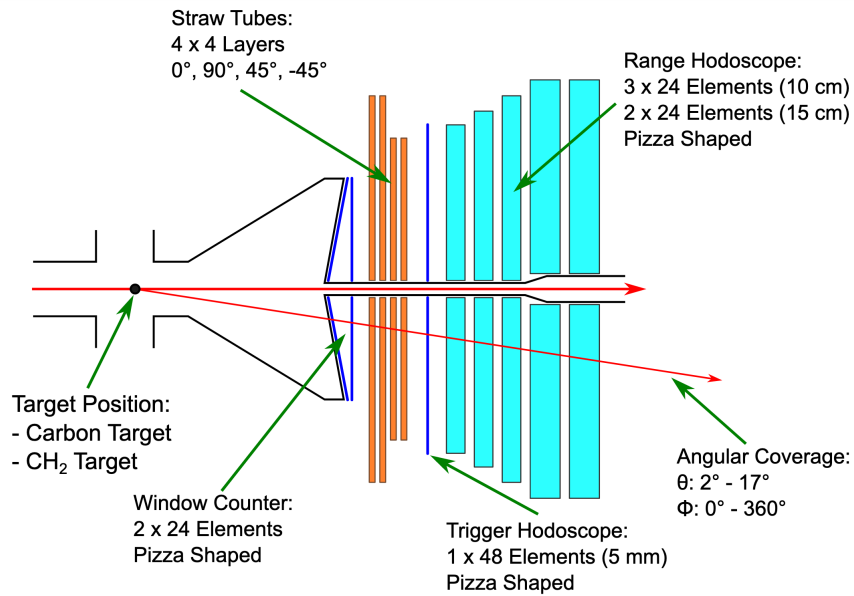


Figure 3.3.: Schematic of the Wasa forward detector [25, p.28].

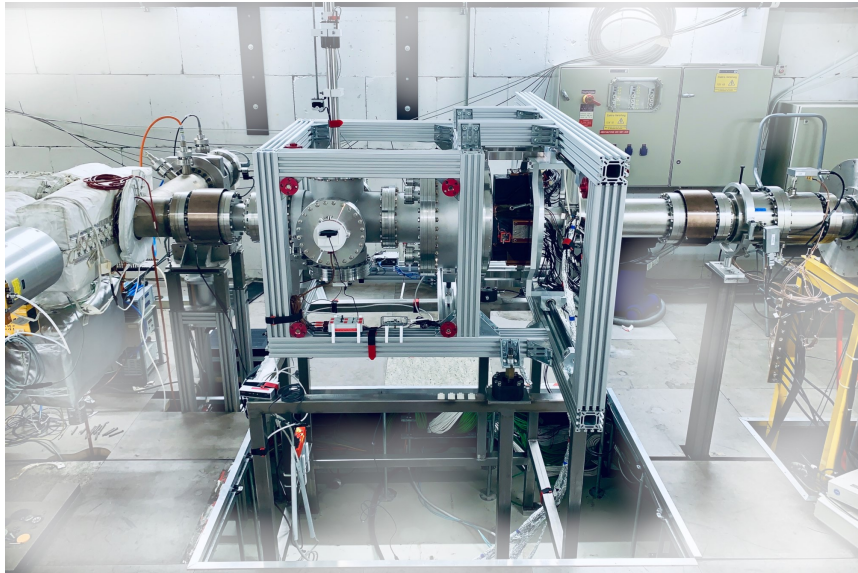


Figure 3.4.: The new JePo polarimeter installed in the ring [7].

4. Data Analysis

In this chapter, a detailed analysis of data taken during the first precursor run in 2018, in terms of spin tune ν_s , phase φ_s and horizontal polarisation ϵ_H , is presented. The ROOT data analysis framework is used for the analysis [27].

4.1. Measurement Principle

The polarised source provides only vertically polarised beam that is accelerated in the cyclotron. When the fully vertically polarised beam is injected into COSY, beam preparation takes place, including bunching and cooling. Afterwards, the solenoid rotates the polarisation into the horizontal plane and the polarisation starts to precess with the spin tune frequency. At this point, the phase feedback system is started. Afterwards, the RF Wien Filter is switched on and the frequency f_{WF} is set to the precession frequency f_{prec} , while fixing the relative phase between the spin tune and the RF Wien Filter, and the vertical polarisation builds up. A schematic of the measurement principle can be seen in Figure 4.1. However, unless specifically indicated, this thesis deals with data that is taken with the feedback system turned off when the RF Wien Filter is switched on. Observed effects are discussed in section 4.8. The data is provided in so-called ROOT trees. A detailed description of the root trees is listed in Table 4.1. To determine the polarisation precessing frequency and the horizontal polarisation, an integer turn number $n \in \mathbb{Z}$ is assigned to each event. The timing takes the COSY RF cavity as a reference. In this work, only polarised deuteron data is analysed.

4.2. Polarimetry

The general coordinate system, used in this thesis can be seen in Figure 4.2. For the purpose of a polarimeter, the WASA detector is subdivided into four different detectors named up, down, left and right detector. These detectors refer to the relative position seen by the beam. The up, down, left and right detectors' centers are placed at polar angles of $\phi \approx 90^\circ, 270^\circ, 0^\circ$ and 180° respectively, each covering a polar angle range of $\Delta\Phi \approx 90^\circ$.

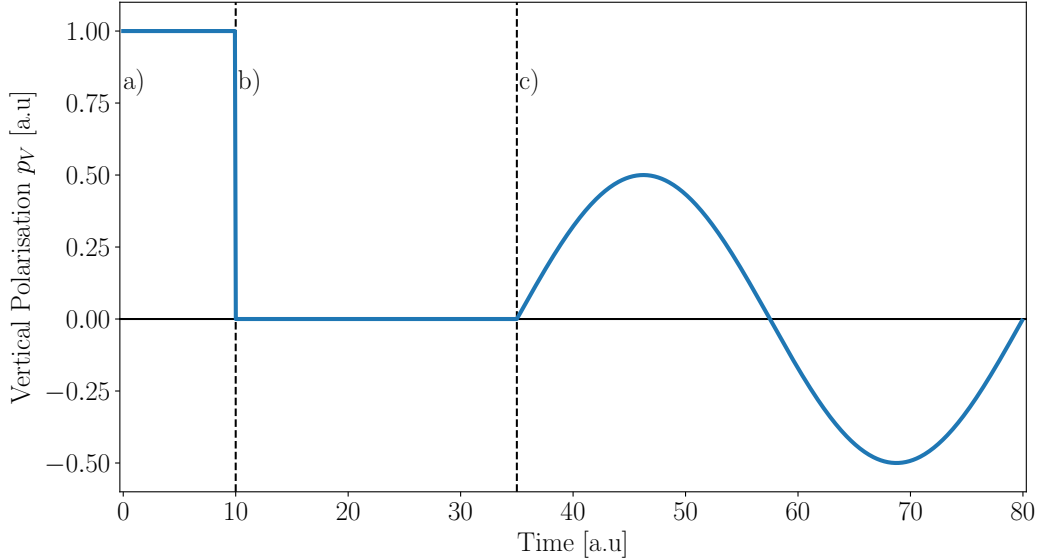


Figure 4.1.: Measurement principle: **a)** Beam preparation, including bunching and cooling. **b)** The RF Solenoid turns the polarisation into the horizontal plane ($\epsilon_V = 0$), feedback preparation takes place. **c)** The RF Wien Filter is switched on and the frequency is set to the polarisation precession frequency $f_{WF} = f_{prec}$, while adjusting and maintaining the relative phase between the polarisation precession and the RF Wien Filter. However, unless specifically indicated, this thesis deals with data, taken with the feedback system turned off, when the RF Wien Filter is switched on. When the RF Wien Filter is switched on, the vertical polarisation accumulates due to the EDM and systematics.

Table 4.1.: Root Tree Information.

Name	Data Type	Meaning
polstate	int	initial polarisation of data 1: up 2: down 15: unpolarised
tir	float	time in run
cycle	int	cycle of data
counter	int	detector 0: up 1: right 2: down 3: left
tic	float	time in cycle
turn	int	turn number
ph_cosy	float	phase relative to cosy rf, <i>i.e.</i> position within one turn
ph_sol	float	phase relative to solenoid rf
ph_wf	float	phase relative to Wien Filter RF

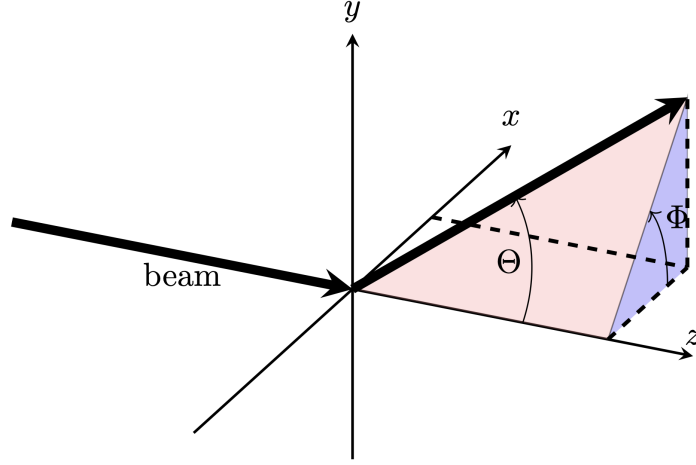


Figure 4.2.: Coordinate system used in this thesis. The bold arrows denote the beam direction and the track of a scattered particle. The angles Φ and Θ are the polar angle and the azimuthal angle, respectively [28].

The elastic differential cross section for vector polarised deuterons scattering from a spin 0 (carbon) target is given by [29]

$$\left(\frac{d\sigma_{\text{pol}}^{dC}(\Theta, \Phi)}{d\Omega} \right) = \left(\frac{d\sigma_0(\Theta)}{d\Omega} \right) \cdot \left(1 + \frac{3}{2} P_V A_y(\Theta) \cos(\Phi) - \frac{3}{2} P_H A_y(\Theta) \sin(\Phi) \right), \quad (4.1)$$

ignoring tensor polarisation, where the polar and the azimuthal angles are given by Φ and Θ and $d\Omega$ is the differential solid angle. The magnitude of the vertical and the in-plane beam polarisation are given by P_V and P_H , respectively. The vector analysing power $A_y(\Theta)$ is a property of the elastic scattering between the carbon target and the deuteron beam. $\frac{d\sigma_0(\Theta)}{d\Omega}$ is the differential cross section for an unpolarised beam and depends only on the azimuthal angle. The number of detected events per time unit and solid angle is given by

$$\frac{dN(\Theta, \Phi)}{d\Omega dt} = \mathcal{L} \cdot \alpha(\Theta, \Phi) \cdot \left(\frac{d\sigma_0(\Theta)}{d\Omega} \right) \cdot \left(1 + \frac{3}{2} P_V A_y(\Theta) \cos(\Phi) - \frac{3}{2} P_H A_y(\Theta) \sin(\Phi) \right), \quad (4.2)$$

where $\alpha(\Theta, \Phi)$ is the geometrical acceptance of the detector and \mathcal{L} the integrated luminosity of the deuteron beam. An expression for the event rate is obtained by integrating over the solid angle, assuming that the acceptance is

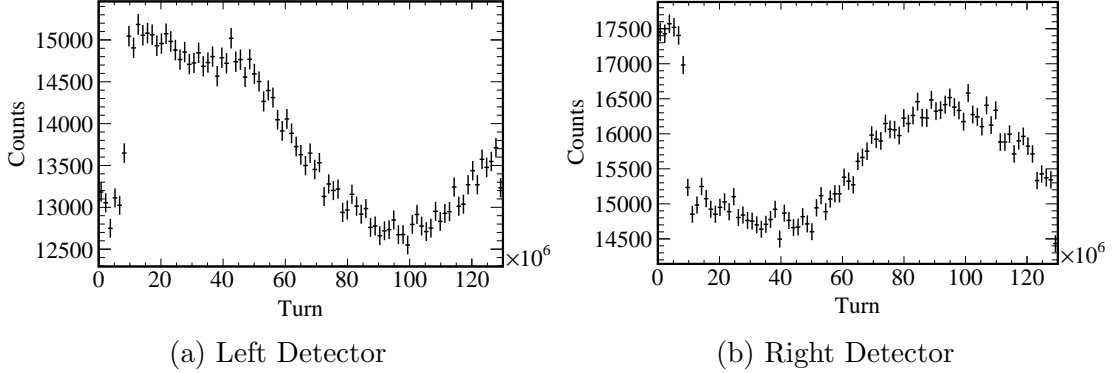


Figure 4.3.: Integrated Count Rates as a function of turn numbers in COSY.

the same for each detector, yielding

$$\frac{dN}{dt} = \int_{\Omega} \frac{dN(\Theta, \Phi)}{d\Omega dt} d\Omega, \quad (4.3)$$

$$\frac{dN_{\text{Up}}}{dt} = \mathcal{L} \cdot \alpha \cdot \bar{\sigma}_{0\text{U}} \cdot \left(1 - \frac{3}{2} P_H \overline{A}_y\right), \quad (4.4)$$

$$\frac{dN_{\text{Down}}}{dt} = \mathcal{L} \cdot \alpha \cdot \bar{\sigma}_{0\text{D}} \cdot \left(1 + \frac{3}{2} P_H \overline{A}_y\right), \quad (4.5)$$

$$\frac{dN_{\text{Left}}}{dt} = \mathcal{L} \cdot \alpha \cdot \bar{\sigma}_{0\text{L}} \cdot \left(1 + \frac{3}{2} P_V \overline{A}_y\right), \quad (4.6)$$

$$\frac{dN_{\text{Right}}}{dt} = \mathcal{L} \cdot \alpha \cdot \bar{\sigma}_{0\text{R}} \cdot \left(1 - \frac{3}{2} P_V \overline{A}_y\right), \quad (4.7)$$

where $\bar{\sigma}_{0X}$ is the integrated spin-independent cross section and \overline{A}_y the weighed average analysing power, which is assumed to be the same for each detector. Due to the angular precession of the horizontal polarisation (eq. 2.12), P_H can be written as

$$P_H(t) = P_{xz} \sin(\Omega_s t + \varphi_s). \quad (4.8)$$

The angular frequency, the phase and the magnitude of the horizontal spin precession are denoted by $\Omega_s = 2\pi\nu_s f_{\text{rev}}$, φ_s and $P_{xz} = \sqrt{p_x^2 + p_y^2}$. The angular frequency in COSY is roughly $f_{\text{prec}} = |\nu_s| f_{\text{rev}} \approx 0.16 \cdot 750 \text{ kHz} = 120 \text{ kHz}$. The detector on the other side can only handle data rates of roughly 5000 Hz. Therefore a simple fit with ν_s as a parameter is not possible, as only one event is detected per 24 spin revolutions. Members of the JEDI collaboration developed methods to measure the spin tune with highest precision $\mathcal{O}(10^{-10})$.

4.3. Vertical Polarisation

The vertical polarisation can be determined by using time integrated count rates, measured in the left (eq. 4.6) and right detector (eq. 4.7). A left-right asymmetry ϵ_V is defined to calculate the vertical polarisation

$$\epsilon_V = \frac{N_L - N_R}{N_L + N_R} = \frac{3}{2} P_y \overline{A}_y, \quad (4.9)$$

where $\overline{\sigma}_{0R} = \overline{\sigma}_{0L}$ is assumed.¹ Note that the unpolarised cross section, acceptance and especially luminosity cancel out, which makes this asymmetry independent of beam parameters (except for the vertical polarisation P_y). Assuming Poisson statistics for time intergrated counts in the left and right detectors ($\sigma_{\text{bin}} = \sqrt{N}$), the statistical uncertainty of ϵ_V is given by

$$\sigma_{\epsilon_V} = \frac{2\sqrt{N_L N_R}}{(N_L + N_R)^{3/2}}. \quad (4.10)$$

If the analysing power \overline{A}_y is known, the vertical polarisation P_y can be determined by rearranging eq. 4.9. The integrated counts in the individual detectors (left and right) can be seen in Figure 4.3.

The left-right asymmetry ϵ_V according to eq. 4.9 is shown in Figure 4.4. The steps, described in section 4.1, can be easily distinguished. Data acquisition starts shortly before the beam polarisation is rotated with the rf solenoid in the horizontal plane at roughly 10×10^6 turns. Afterwards, the vertical polarisation is zero, as the horizontal polarisation is maximal. When the RF Wien Filter is switched on at roughly 50×10^6 turns, the vertical polarisation accumulates.

However, the build-up is not a clean EDM signal, as systematic effects like misaligned magnets create fake EDM signals. Studies of systematic effects are currently ongoing at JEDI. In Figure 4.5 the average vertical spin component build-up is plotted for simulated offsets of the beam position including vertically randomly distributed quadrupole misalignments. For larger beam offsets, the strengths of the EDM signal (η from eq. 2.3) becomes indistinguishable from a build-up, caused by misalignments. The dashed line denotes the location for which the false signal by misalignments is equal to an EDM strength of $\eta = 10^{-4}$. In order to be sensitive to even lower EDM strengths, a stable and precise orbit is crucial for an EDM experiment [31, p.157-158].

¹Small differences in $\overline{\sigma}_{0R}$ and $\overline{\sigma}_{0L}$ lead to a bias and distortion of the vertical polarisation. However, the proportionality between ϵ_V and p_H remains. A more precise determination of p_H is based on the crossratio of up- and down polarised data [30].

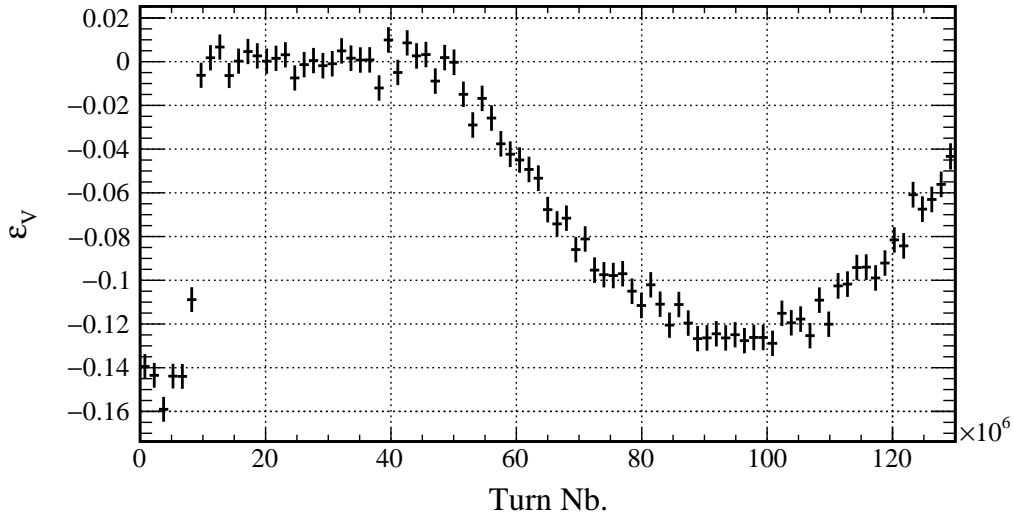


Figure 4.4.: Left - Right Asymmetry ϵ_V as a function of turn numbers in COSY. At 50×10^6 turns, the RF Wien Filter is switched on and the vertical polarisation accumulates.

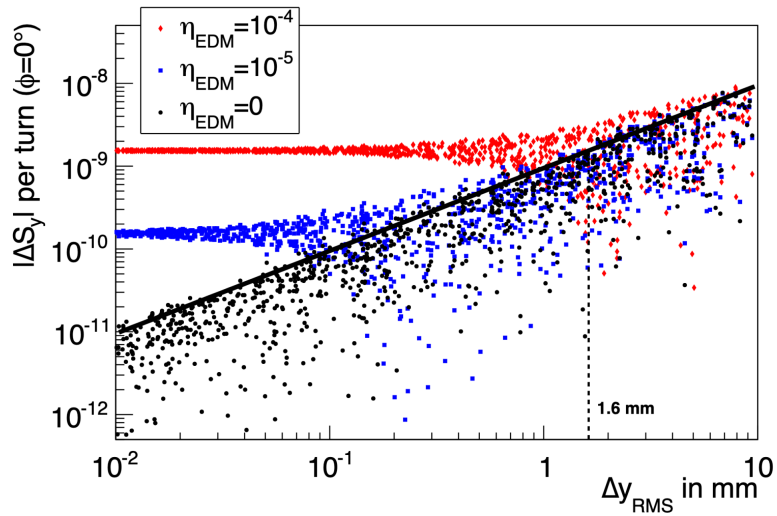


Figure 4.5.: Polarisation build-up per turn as a function of the beam offset in y direction from the nominal orbit, simulated with Gaussian quadrupole misalignments in COSY. Additionally, further EDM strengths are considered. A precise orbit is crucial for an EDM experiment to be sensitive to low EDM strengths. The dashed line denotes the location for which a signal due to quadrupole misalignment is equal to an EDM strength of $\eta = 10^{-4}$ [31, p.158].

The analytical work from eq. 4.11 to 4.20 is taken from former IKP student Dennis Eversmann's PhD Thesis *High Precision Spin Tune Determination at the Cooler Synchrotron in Jülich* [32, p.41-46].

4.4. Mapping Method

A first method to determine the amplitude ϵ_H and the phase φ_s of the spin precession is the so-called mapping method. The idea is to map all detected events into one single oscillation period. The basic principle can be seen in Figure 4.6. The upper plot shows the true spin tune oscillation together with data samples. The entire cycle is divided into macroscopic time intervals of equal length (1.5×10^6 turns (≈ 2 s), lower left plot). In each time window, all events are mapped into one oscillation period assuming an arbitrary chosen spin tune. A clear oscillation unfolds as soon as the true spin tune value is chosen (lower right plot).

A great advantage of the mapping method is its independence of beam properties (except the polarisation), *i.e.* beam luminosity and acceptance of the detector, as it uses combined detector rates, measured by the up and down detector.

4.4.1. Spin Phase Advance φ_s

To each recorded event, a turn number n is assigned. The spin phase advance of an arbitrarily assumed spin tune ν is given by

$$\varphi_s(n) = 2\pi\nu n. \quad (4.11)$$

The spin phase advance is mapped into a 4π interval via the modulo operator

$$\varphi_s(n) = \varphi_s(n) \bmod 4\pi. \quad (4.12)$$

This procedure is repeated for each microscopic time interval for the up- and down detector individually. In Figure 4.7, two examples of the mapped spin phase advance according to eq. 4.12 are shown for two different assumed spin tunes. The statistical error of each bin is given by $\sigma_{\text{bin}} = \sqrt{N}$, as Poisson statistics is assumed. In Figure 4.7a a clear oscillation pattern can be seen, which indicates that the assumed spin tune is close to the true spin tune.

On the other hand, in Figure 4.7b, no oscillation pattern is observable, as the assumed spin tune is not consistent with the true spin tune. A least square fit is performed to data to calculate the phase $\varphi_{s,\text{fit}}$ and the amplitude N_{amp} of

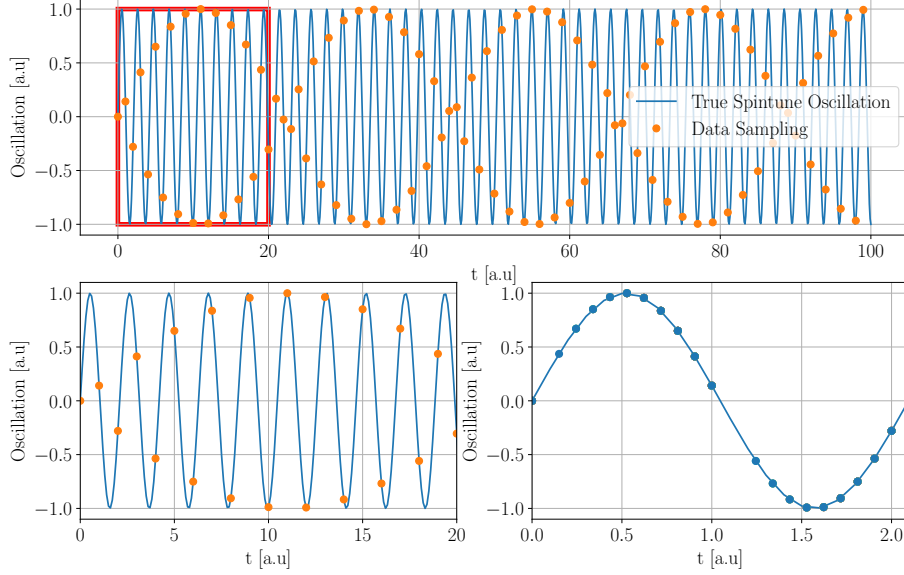


Figure 4.6.: The basic principle of the mapping method. The upper plot shows the true spin tune oscillation with data sampling. The lower plot shows the upper plot for a macroscopic time interval (red box). The lower right plot shows the result of the mapping method for $\nu_{\text{assumed}} = \nu_{\text{true}}$.

the oscillation

$$N(\varphi_s) = N_{\text{const}}^{\nu_s} + N_{\text{amp}}^{\nu_s} \sin(\varphi_s^{\nu_s} + \varphi_{s,\text{fit}}^{\nu_s, \text{fix}}). \quad (4.13)$$

The results of the least square fits shown in Figure 4.7a are listed in table 4.2. The oscillations of the two detectors should be phase shifted by π . This becomes obvious in eq. 4.4 and 4.5, as the sign of the term, describing the precession of the polarisation, changes. The phase shift for the data shown in Figure 4.7a is given by $\Delta\phi_s = |2.45| + |-0.56| = 3.01 \pm 0.13$, which is compatible with a phase shift of π . As it can be seen in eq. 4.4 and 4.5, the rates, measured in separate detectors depend on the acceptance of the detector

Table 4.2.: Results of the least square fits, shown in Figure 4.7a.

	Up Detector	Down Detector
N_{const}	339.34 ± 2.91	344.91 ± 2.94
N_{amp}	46.82 ± 4.09	47.71 ± 4.14
$\varphi_{s,\text{fit}}$	-0.56 ± 0.09	2.45 ± 0.09
χ^2/ndf	$39.28 / 37$	$40.63 / 37$

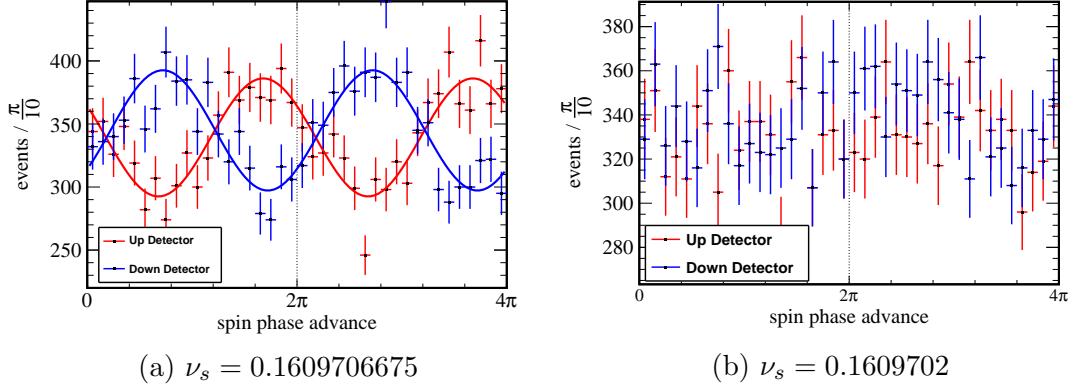


Figure 4.7.: The spin phase advance according to eq. 4.12 for the up- and down detector individually for two different assumed spin tunes ν in a macroscopic time interval. If the assumed spin tune corresponds to the true spin tune, an oscillation pattern unfolds, which is fitted according to eq. 4.13. The fit results are given in table 4.2.

and beam luminosity. Therefore, the amplitude in eq. 4.13 is only proportional to the true horizontal polarisation of the precessing polarisation. In the next section a method is presented that uses an asymmetry of the up and down detector to cancel out this effect.

4.4.2. True Amplitude & Phase

In order to determine the true amplitude and phase of the horizontal polarisation precession, the following new count rates, based on eq. 4.12, are defined

$$N_X^\pm(\varphi_s) = \begin{cases} N_X(\varphi_s) \pm N_X(\varphi_s + 3\pi) & \text{for } 0 \leq \varphi_s < \pi \\ N_X(\varphi_s) \pm N_X(\varphi_s + \pi) & \text{for } \pi \leq \varphi_s < 2\pi \end{cases} \quad (4.14)$$

where X is either the up- or down detector. By rearranging the count rates, a new up - down asymmetry $\epsilon_H(\varphi_s)$ can be defined, in analogy to the vertical asymmetry in eq. 4.9

$$\begin{aligned} \epsilon(\varphi_s) &= \frac{N_U^-(\varphi_s) - N_D^-(\varphi_s)}{N_U^+(\varphi_s) + N_D^+(\varphi_s)} \\ &= \frac{3}{2} p_{xz} \frac{\overline{\sigma_{0U} A_y} - \overline{\sigma_{0D} A_y}}{\overline{\sigma_{0U}} + \overline{\sigma_{0D}}} \sin(\varphi_s + \varphi). \end{aligned} \quad (4.15)$$

The vertical asymmetry is shown in Figure 4.8 for a macroscopic time interval. It is proportional to the sine of the spin phase advance. Performing a least

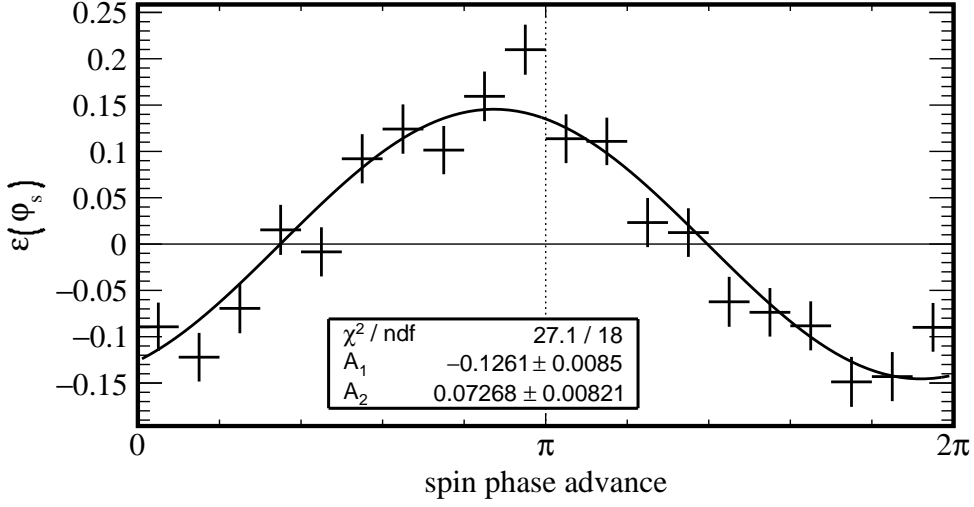


Figure 4.8.: Vertical asymmetry $\epsilon(\varphi_s)$ fitted with eq. 4.16 to extract the horizontal amplitude ϵ_H and the phase φ_s .

square fit according to

$$\epsilon_H(\varphi_s) = A_1 \sin(\varphi_s) + A_2 \cos(\varphi_s) \quad (4.16)$$

yields the amplitude and the phase of the precession. Both can be calculated via

$$\epsilon = \sqrt{A_1^2 + A_2^2} = \sqrt{-0.1261^2 + 0.07268^2} = 0.1455 \pm 0.0084 \quad (4.17)$$

$$\varphi = \text{atan2}(A_2, A_1) = \text{atan2}(-0.1261, 0.07268) = (-1.048 \pm 0.057) \text{ rad} \quad (4.18)$$

where atan2 denotes the arctangent [33]. In eq. 4.17 and 4.18 the numbers from Figure 4.8 are used as an example. However, it was shown that the horizontal amplitude is biased for small amplitudes. A new method, based on confidence intervals and Bayes' theorem was developed in reference [34]. The statistical errors of the amplitude and the phase are calculated via Gaussian error propagation

$$\sigma_\epsilon^2 = \frac{A_1^2 \sigma_{A_1}^2 + A_2^2 \sigma_{A_2}^2}{A_1^2 + A_2^2}, \quad (4.19)$$

$$\sigma_\varphi^2 = \frac{A_2^2 \sigma_{A_1}^2 + A_1^2 \sigma_{A_2}^2}{(A_1^2 + A_2^2)^2}. \quad (4.20)$$

In Figure 4.9a the amplitude according to eq. 4.17 is shown as a function of time and assumed spin tune, where the color denotes the amplitude. The

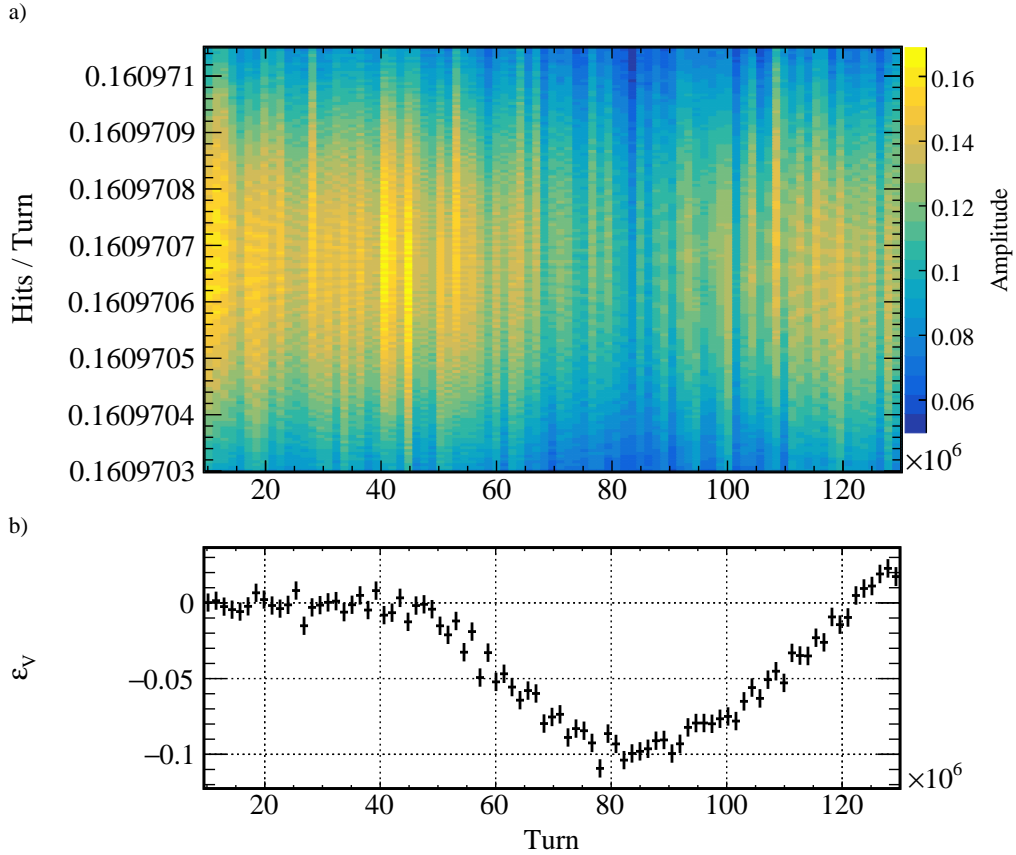


Figure 4.9.: **a)** Amplitude spectra, computed with the mapping method according to eq. 4.17. A spin tune range from 0.1609703 to 0.16097105 with $\Delta\nu = 7.5 \cdot 10^{-9}$ (100 spin tune bins) is scanned in 87 time bins.

b) Vertical polarisation ϵ_V for comparison.

analysis starts from 9.5×10^6 turns, as before the beam is vertically polarised and thus shows no precession in the horizontal plane. As soon as the Wien Filter is switched on, the vertical polarisation increases and the amplitude of the horizontal polarisation decreases. For each point in Figure 4.9 a phase can be calculated which is used to calculate the spin tune, see section 4.6. An example of the phase for different assumed spin tunes is shown in Figure 4.14.

The analytical work from eq. 4.22 to 4.30 is taken from former IKP student Dennis Eversmann's PhD Thesis *High Precision Spin Tune Determination at the Cooler Synchrotron in Jülich* [32, p.47-50].

4.5. Fourier Method

In this section, a second method of computing the horizontal polarisation ϵ_H and the phase φ_s of the precession is presented, which is based on the regular Fourier transform. The Fourier transform $f(\omega)$ of a continuous 1-dimensional periodic probability density function $\hat{f}(t) = A \cos(\omega_s t + \phi_s)$, where $\omega_s = 2\pi\nu_s$, is given by

$$f(\omega) = \int_{-\infty}^{\infty} \hat{f}(t) e^{it\omega} dt, \quad (4.21)$$

transforming the periodic probability density function into the frequency space ω . Computing $f(\omega)$ would result in a delta distribution at ω_s . As the timing of events is not a continuous function and the detector is placed at a discrete place in COSY, the Fourier transform of a continuous function does not apply. Therefore the so-called Discrete Turn Fourier Transform is used, which is explained in more detail in the following.

The basic principle of the Fourier method is very similar to the principle explained in section 4.4. The only difference is the discrete Fourier transformation which results in a peak at the true spin tune frequency as shown in Figure 4.10.

4.5.1. Discrete Turn Fourier Transform

The Discrete Turn Fourier Transform (DTFT) is based on the assignment of a discrete turn number n to each event. Therefore $\hat{f}(t)$ in eq. 4.21 becomes mathematically a discrete delta comb, which consists of Dirac delta functions $\delta(t - n/f_{\text{RF}})$, where f_{RF} denotes the radio frequency of the cavity

$$\begin{aligned} f(\omega) &= \int_{-\infty}^{\infty} \sum_{n=0}^{\infty} \hat{f}(t) \delta\left(t - \frac{n}{f_{\text{RF}}}\right) e^{-it\omega} dt \\ &= \sum_{n=0}^{\infty} \hat{f}[n] e^{\frac{-in\omega}{f_{\text{RF}}}} \\ &= \sum_{n=0}^{\infty} \hat{f}[n] e^{\frac{-i2\pi n\omega}{\omega_{\text{RF}}}} \end{aligned} \quad (4.22)$$

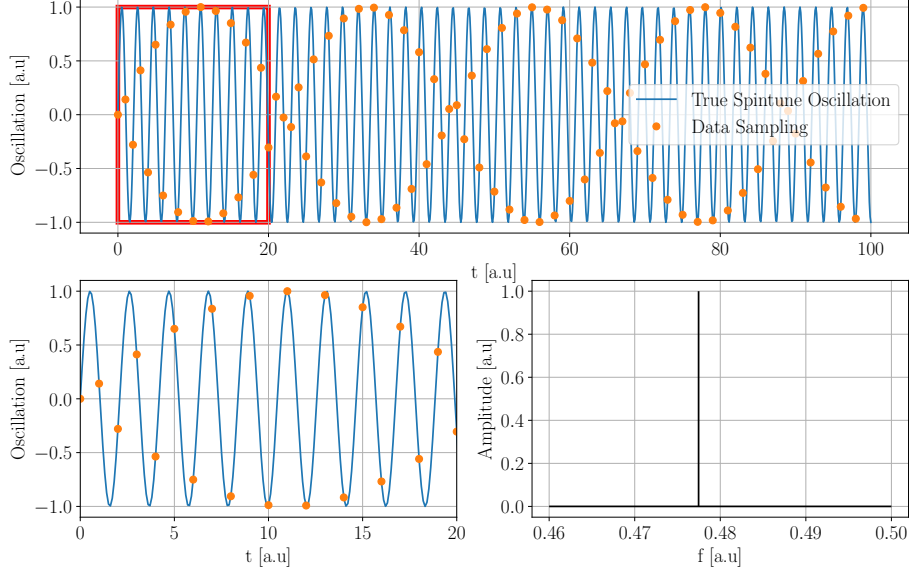


Figure 4.10.: The basic principle of the Fourier method. The upper plot shows the true spin tune oscillation with data sampling. The lower plot shows the upper plot for a macroscopic time interval. The lower right plot shows the Fourier spectra of data in a macroscopic time interval. A peak appears at the true spin tune position.

where the square brackets denote a discrete argument of \hat{f} . With the relation $\nu = \omega/\omega_{\text{RF}}$, eq. 4.22 gets

$$f(\nu) = \sum_{n=0}^{\infty} \hat{f}[n] e^{-i2\pi n \cdot \nu} \quad (4.23)$$

with $\hat{f}[n] = A \cos(2\pi \nu_s n + \varphi_s)$.

As the measurement time interval is not infinite, it is useful to define a rectangular function $w[n]$

$$\hat{w}[n] = \begin{cases} 0 & n < 0 \\ 1 & 0 \leq n < N \\ 0 & n \geq N \end{cases} \quad (4.24)$$

where N denotes the total number of events in a finite time interval. Multiplying in turn space $\hat{g}[n] = \hat{f}[n] \cdot \hat{w}[n]$ corresponds to a convolution in the spin tune domain $g[\nu] = f[\nu] * w[\nu]$

$$\begin{aligned}
 g(v) &= f(v) * w(v) = (f * w)(v) \\
 &= \int_{-\infty}^{\infty} f(v - \lambda)w(\lambda)d\lambda \\
 &= \sum_{n=0}^{\infty} \hat{f}[n]\hat{w}[n]e^{-i2\pi n \cdot v} \\
 &= \sum_{n=0}^{N-1} \hat{g}[n]e^{-i2\pi n \cdot v} \\
 \Rightarrow g_{\nu_k} &= \sum_{n=0}^{N-1} \hat{g}[n] [\cos(2\pi n \nu_k) - i \sin(2\pi n \nu_k)] \quad (4.25)
 \end{aligned}$$

In the last step, Euler's formula is used. Additionally, ν_k is introduced, as the difference between two adjacent values of ν is not infinitesimally small. Therefore, ν_k becomes discrete. ν_k is an element of the scanned spin tune range $\{\nu_{\min}, \nu_{\max}\}$ with $k \in \{1, \dots, k_{\max}\}$

$$\begin{aligned}
 \nu_k &= \nu_{\min} + \Delta\nu(k) \cdot (\nu_{\max} - \nu_{\min}), \quad (4.26) \\
 \Delta\nu(k) &= \frac{k - 1}{k_{\max} - 1}.
 \end{aligned}$$

The prefactor $\hat{g}[n]$ represents the randomly distributed turn events and is determined, based on the probability function $\hat{f}[n]$ in eq. 4.23. $\hat{g}[n]$ is one, when the turn number n corresponds to a detected event $n = n(n_{\text{ev}})$

$$\hat{g}[n] = \begin{cases} 1 & \text{for } n = n(n_{\text{ev}}) \\ 0 & \text{else.} \end{cases} \quad (4.27)$$

Therefore, eq. 4.25 reduces to

$$g_{\nu_k} = \sum_{n(n_{\text{ev}})=1}^{N_{\text{ev}}} \cos(2\pi \nu_k n(n_{\text{ev}})) - i \sin(2\pi \nu_k n(n_{\text{ev}})), \quad (4.28)$$

where N_{ev} is the total number of events ($n_{\text{ev}} \in \{1, N_{\text{ev}}\}$). The discrete Fourier parameters a_{ν_k} and b_{ν_k} are given by the real and the imaginary part of eq. 4.28

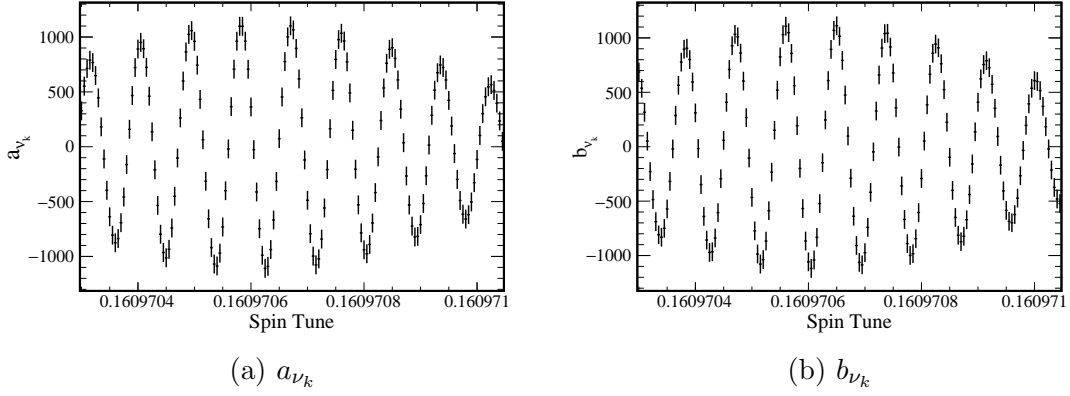


Figure 4.11.: Fourier parameters a_{ν_k} and b_{ν_k} as a function of assumed spin tune, measured by the up detector in a macroscopic time interval. The spin tune ranges from 0.1609703 to 0.16097105 with $\Delta\nu_k = 5 \cdot 10^{-9}$ (150 bins).

respectively

$$a_{\nu_k} = \text{Re}(g_{\nu_k}) = \frac{2}{N_{\text{ev}}} \sum_{n_{\text{ev}}=1}^{N_{\text{ev}}} \cos(2\pi\nu_k n(n_{\text{ev}})), \quad (4.29)$$

$$b_{\nu_k} = \text{Im}(g_{\nu_k}) = \frac{2}{N_{\text{ev}}} \sum_{n_{\text{ev}}=1}^{N_{\text{ev}}} -\sin(2\pi\nu_k n(n_{\text{ev}})). \quad (4.30)$$

The factor $2/N_{\text{ev}}$ takes the normalisation based on Parseval's theorem into account [35]. The statistical uncertainty of the Fourier parameters is given by

$$\sigma_{a_{\nu_k}} = \frac{2}{N_{\text{ev}}} \sqrt{\sum_{n_{\text{ev}}=1}^{N_{\text{ev}}} \cos^2(2\pi\nu_k n(n_{\text{ev}}))}, \quad (4.31)$$

$$\sigma_{b_{\nu_k}} = \frac{2}{N_{\text{ev}}} \sqrt{\sum_{n_{\text{ev}}=1}^{N_{\text{ev}}} \sin^2(2\pi\nu_k n(n_{\text{ev}}))}. \quad (4.32)$$

A derivation for eq. 4.31 and 4.32 is given in section A.1. An example of the Fourier parameters as a function of the assumed spin tune in a macroscopic time interval is shown in Figure 4.11.

4.5.2. Amplitude & Phase

The amplitude and the phase of the Fourier transform can be computed with the Fourier parameters

$$\epsilon_{v_k} = |g_{v_k}| = \sqrt{\text{Im}(g_{v_k})^2 + \text{Re}(g_{v_k})^2} = \sqrt{a_{v_k}^2 + b_{v_k}^2}, \quad (4.33)$$

$$\varphi_{v_k} = \arg(g_{v_k}) = \text{atan2}(\text{Im}(g_{v_k}), \text{Re}(g_{v_k})) = \text{atan2}(b_{v_k}, a_{v_k}). \quad (4.34)$$

The statistical uncertainties are given by Gaussian error propagation

$$\sigma_{\epsilon_{v_k}}^2 = \frac{a_{v_k}^2 \sigma_{a_{v_k}}^2 + b_{v_k}^2 \sigma_{b_{v_k}}^2}{a_{v_k}^2 + b_{v_k}^2}, \quad (4.35)$$

$$\sigma_{\varphi_{v_k}}^2 = \frac{b_{v_k}^2 \sigma_{a_{v_k}}^2 + a_{v_k}^2 \sigma_{b_{v_k}}^2}{(a_{v_k}^2 + b_{v_k}^2)^2}. \quad (4.36)$$

In Figure 4.12 two examples of the amplitude of the Fourier transform are shown, measured by the up detector in two different macroscopic time intervals. A clear peak around the estimated spin tune is visible. Comparing both spectra, it can be seen that the amplitudes differ because the horizontal polarisation changes with time. Using eq. 4.4 and 4.5, it can be calculated that the amplitudes in the up and down detector (A_{\uparrow} and A_{\downarrow}) of the Fourier spectra are given by

$$A_{\uparrow}(\nu = \nu_s) = A_{\downarrow}(\nu = \nu_s) = \epsilon_H, \quad (4.37)$$

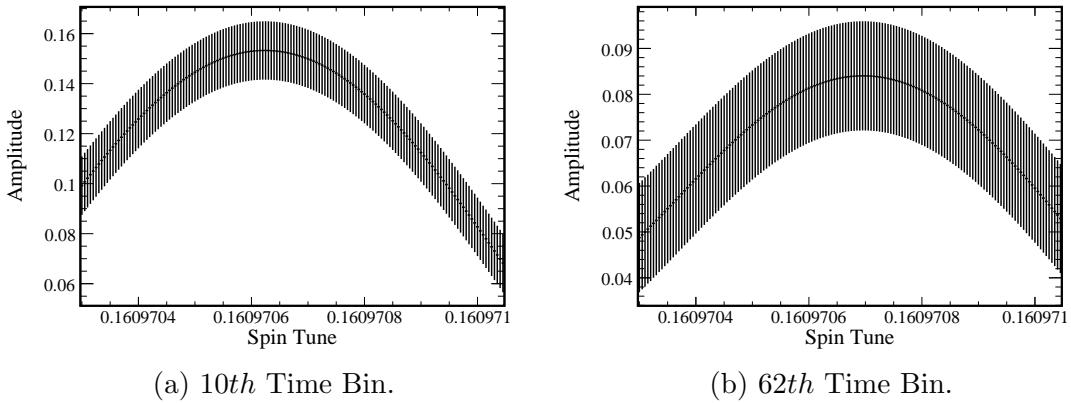


Figure 4.12.: Fourier Amplitudes according to eq. 4.33 for two different time bins. Both spectra are measured by the up detector. The scanned spin tune ranges from 0.1609703 to 0.16097105 with $\Delta\nu_k = 5 \cdot 10^{-9}$.

with $\epsilon_H = \frac{3}{2}p_{xz}\overline{A_y}$. A detailed derivation for eq. 4.37 is given in section A.2. A comparison of the horizontal polarisation measured with both detectors and the mapping method is shown in Figure 4.15. The phases measured with the up and down detector can be seen in Figure 4.16.

4.6. Spin Tune Determination

To determine the spin tune as a function of turn number $\nu_s(n)$, a fixed spin tune ν_s^0 and the change of phase for that fixed spin tune, that acts as a baseline, needs to be determined

$$\begin{aligned}
 \frac{\nu_s(n)}{\nu_s^0} &= 1 + \frac{\Delta\nu_s(n)}{\nu_s^0} \\
 &= 1 + \frac{\Delta f_s(n)}{f_s} - \frac{\Delta f_{\text{RF}}(n)}{f_{\text{RF}}} \\
 &= 1 + \frac{1}{2\pi\nu_s^0} \frac{\partial\varphi_s(n)}{\partial n} \\
 \Rightarrow \nu_s(n) &= \nu_s^0 + \frac{1}{2\pi} \frac{\partial\varphi_s(n)}{\partial n}, \tag{4.38}
 \end{aligned}$$

where f_s and f_{RF} denote the spin precession frequency and the RF cavity frequency respectively [36]. The effect of scanning an off spin tune value, changing the phase is shown in Figure 4.13. Assuming, that the blue curve represents the true horizontal precession, it can be seen that for a data sampling frequency (assumed spin tune) which is slightly different than the true frequency, the phase difference (denoted as the arrows) increases with time. As soon as the data sampling frequency corresponds to the true precession frequency, the difference of phase stays constant. The phase φ_s denotes the phase difference between assumed spin tune frequency ν_s^0 and true spin tune frequency ν_s . The effect for real data can be seen in Figure 4.14 for four different assumed spin tunes. The phase in Figure 4.14c shows the most constant behaviour, which makes the assumed spin tune act as the spin tune baseline ν_s^0 . The change of phase is determined by fitting the phase for the fixed spin tune with a polynomial of 8th order, as the change of phase shows an arbitrary behaviour, because of the spin tune frequency potentially changing due to instabilities of power supplies etc. The change of phase with respect to the turn number n is given by

$$\varphi_s = \sum_{i=0}^8 a_i n^i. \tag{4.39}$$

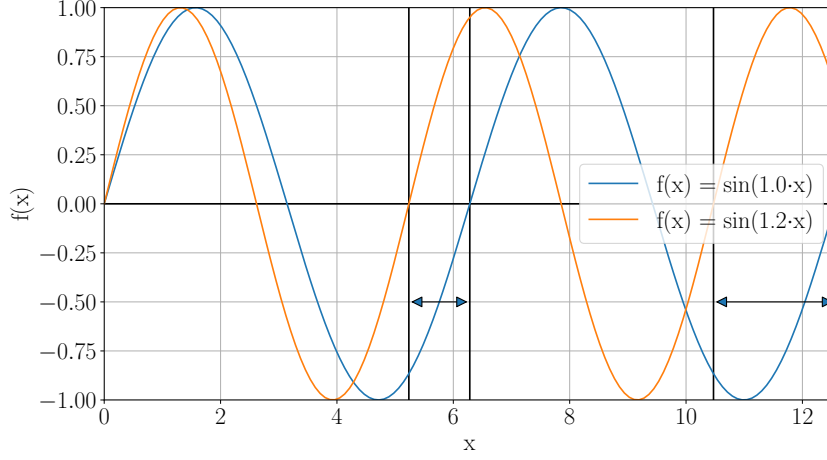


Figure 4.13.: Schematic of the phase shift, if the fixed spin tune is higher (orange curve) than the true spin tune (blue curve). The phase shift is denoted by the arrows. If the assumed spin tune matches the true spin tune, the phase shift stays constant with time.

Taking the derivative leads to

$$\frac{\partial \varphi_s}{\partial n} = \sum_{i=0}^8 a_i n^{i-1} i, \quad (4.40)$$

where a_i denote the fit parameters. The phase, calculated with the single and combined detector method and its least square fits is shown in Figure 4.16. The statistical error including the correlation coefficient ρ_{jk} between the fit parameters a_j and a_k of $\frac{\partial \varphi_s}{\partial n}$ is given by

$$\sigma_{\left(\frac{\partial \phi}{\partial n}\right)}(n)^2 = \sum_{i=0}^8 (n^{i-1} i \sigma_{a_i})^2 + 2 \sum_{j=1}^8 \sum_{\substack{k=1 \\ j \neq k}}^8 t^{j-1} j \cdot t^{k-1} k \cdot \sigma_{a_j} \sigma_{a_k} \rho(a_j, a_k). \quad (4.41)$$

The statistical uncertainty of the spin tune is given by

$$\sigma_{\nu_s}(n) = \frac{1}{2\pi} \sigma_{\left(\frac{\partial \phi}{\partial n}\right)}(n). \quad (4.42)$$

The result of the spin tune is shown in Figure 4.17. Note that calculating the spin tune as a function of time is independent of the particular choice of ν_s^0 , as a different choice of the fixed spin tune is compensated by the change of phase. The statistical sensitivity is in the order of $\mathcal{O}(10^{-10})$ in a measurement time interval of approximately 100 s.

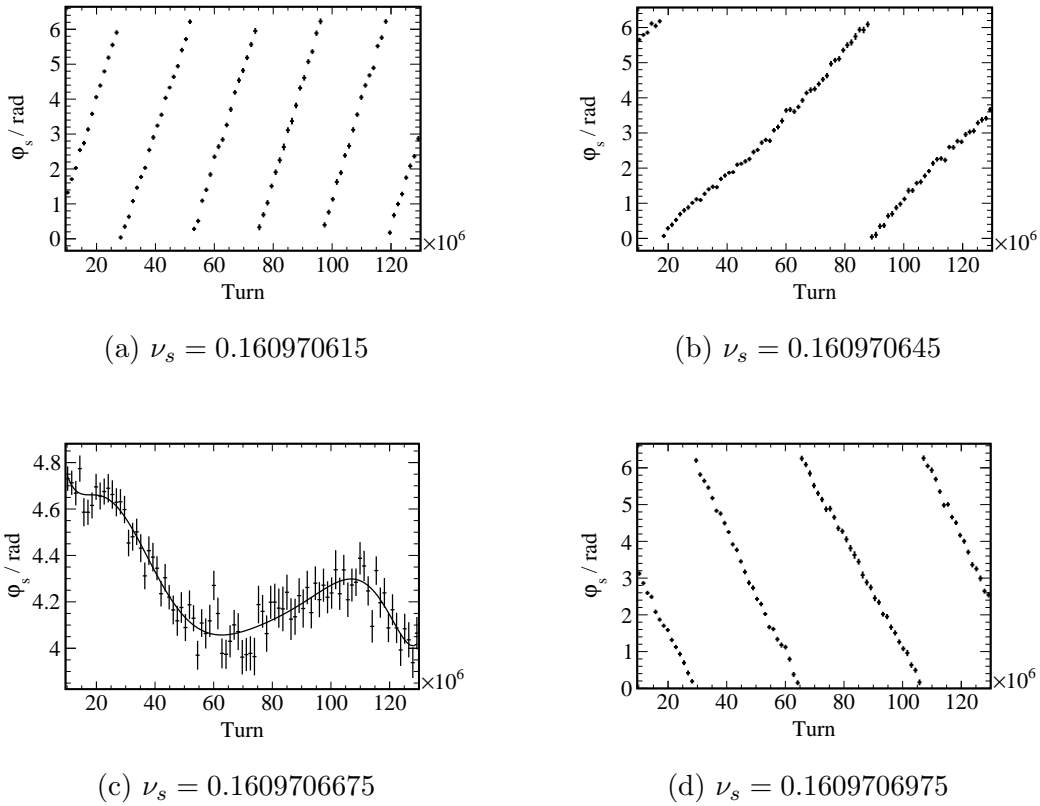


Figure 4.14.: The change of phase for different assumed fixed spin tunes. As soon, as the assumed spin tune corresponds to the true spin tune, the phase shows the most stable behaviour.

4.7. Comparison of the Methods

In this section a comparison between the methods to calculate phase φ_s , horizontal polarisation ϵ_H and spin tune ν_s explained in section 4.4 and 4.5 is given for a cycle where the phase feedback was turned off when turning on the RF Wien Filter. In Figure 4.15 the comparison of the horizontal polarisation is displayed. Figure 4.15a-c show a spectrum according to the mapping method and the single detector Fourier method (up and down), respectively. Figure 4.15d shows the spectra evaluated at the spin tune position, calculated with the combined-detector mapping method. An unexpected and clear difference between those spectra can be seen, even though all three spectra should show the same result. A striking difference of data occurs at roughly 50×10^6 turns, which is the time of switching on the RF Wien Filter. The results of the com-

bined detector mapping method² are always between the results of the single detector method, which are oscillating. A similar behaviour shows the phase (Figure 4.16) and the spin tune (Figure 4.17). The phase determined for the individual detectors fits within their uncertainties until 50×10^6 . Afterwards, a clear deviation occurs, which causes at the same time a deviation when determining the spin tune. The phase calculated with the mapping method shows a small offset. The reason for this offset is unknown. However, the shape of the fit looks similar to the shape of the fit done with the individual detectors. While taking the derivative of the function, a constant offset doesn't matter. Therefore, the shape of the spin tune is not affected by this offset. As explained in more detail in the next section, a mismatch of the electromagnetic fields inside the RF Wien Filter leads to this unexpected behaviour.

4.8. Mismatch of the Wien Filter

The non matching results obtained by the individual detectors method presented in Figure 4.15 - 4.17 are caused by a mismatch of the electromagnetic field inside the RF Wien Filter. Whenever the RF Wien Filter rotates the horizontal polarisation vector, it also excites unintended and unexpected beam oscillations when the Lorentz force at the beam position is not zero. As the Wien Filter kicks the horizontal polarisation periodically with the same frequency ω_{WF} as the rotation of the spintune $\omega_s = 2\pi\nu_s$ and the same phase φ_s , the beam oscillations are expected to be periodic with the same frequency and phase if the phase feedback was switched on during data taking. Additionally, the phase feedback allows to set a constant phase offset φ_0 between the spin tune frequency and the Wien Filter frequency. The beam oscillations have therefore the same phase relation to the precessing spins as the Wien Filter to the precessing spins. Mathematically, a constant phase φ_0 needs to be added to the phase of the spin tune $\varphi_{WF} = \varphi_s + \varphi_0$. The periodic beam oscillations change the number of particles hitting the target when extracting the beam on the target, which leads to an oscillating luminosity

$$\mathcal{L}_{osc} = \mathcal{L}_{COSY} \cdot (1 + a \cos(\omega_{WF}n + \varphi_{WF})), \quad (4.43)$$

where \mathcal{L}_{COSY} is the constant integrated luminosity of COSY without switched on Wien Filter, ω_{WF} is the Wien Filter frequency exciting the beam, a is the corresponding oscillation amplitude and φ_{WF} takes the phase relation between

²Note that the error bars of the combined detector method are smaller by a factor of $\approx \sqrt{2}$. The estimator of uncertainties of the phase, the spin tune and the horizontal polarization scale in good approximation with $1/\sqrt{N}$. The mapping method uses combined rates in the up and down detector which increase the total number of events by a factor of 2, decreasing the uncertainties by a factor of $\sqrt{2}$ [36, 32].

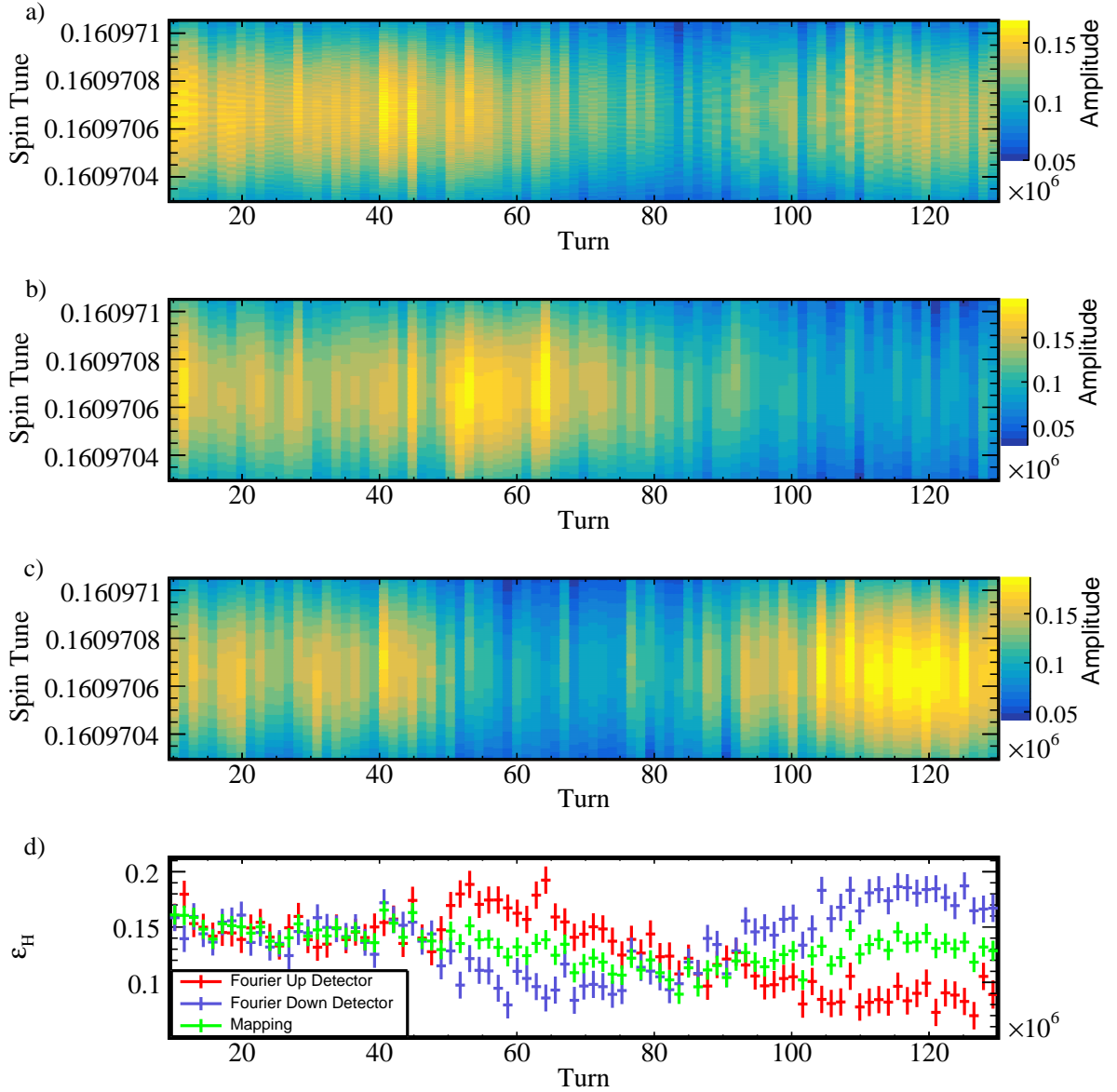


Figure 4.15.: A comparison of the horizontal polarisation. **a)** Mapping method. **b)** Fourier method: Up detector. **c)** Fourier method: Down detector. **d)** Different spectra evaluated at the spin tune position. In each spectra a frequency range in the spin tune domain from 0.1609703 to 0.16097105 is scanned in 150 bins in a time range from 9.5×10^6 to 130×10^6 turns (87 time bins). A clear difference of the result can be seen, when turning on the RF Wien Filter at 50×10^6 turns.

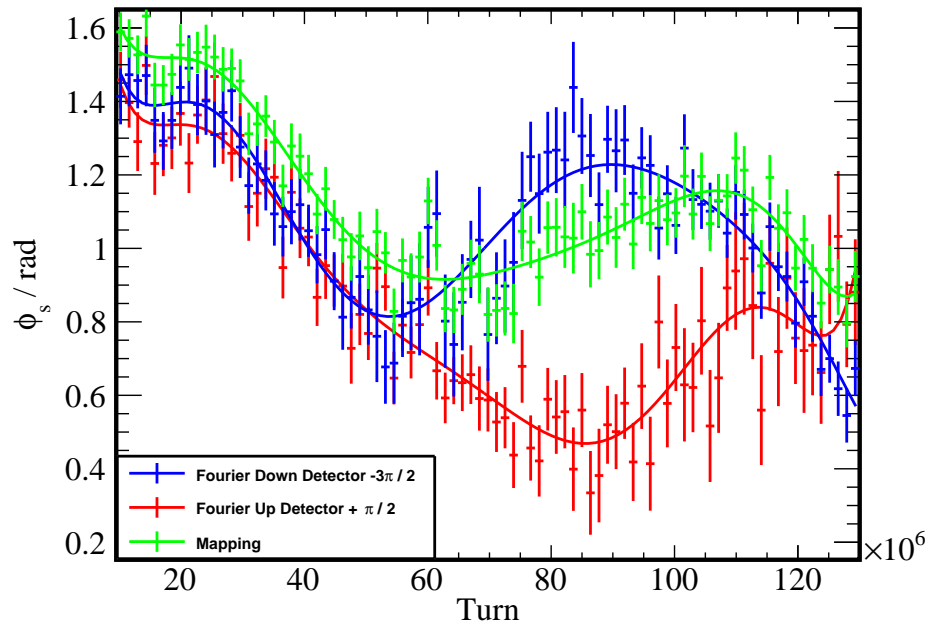


Figure 4.16.: Phase φ_s as a function of turns. The phases determined by the individual detectors is consistent until 50×10^6 , afterwards a deviation occurs.

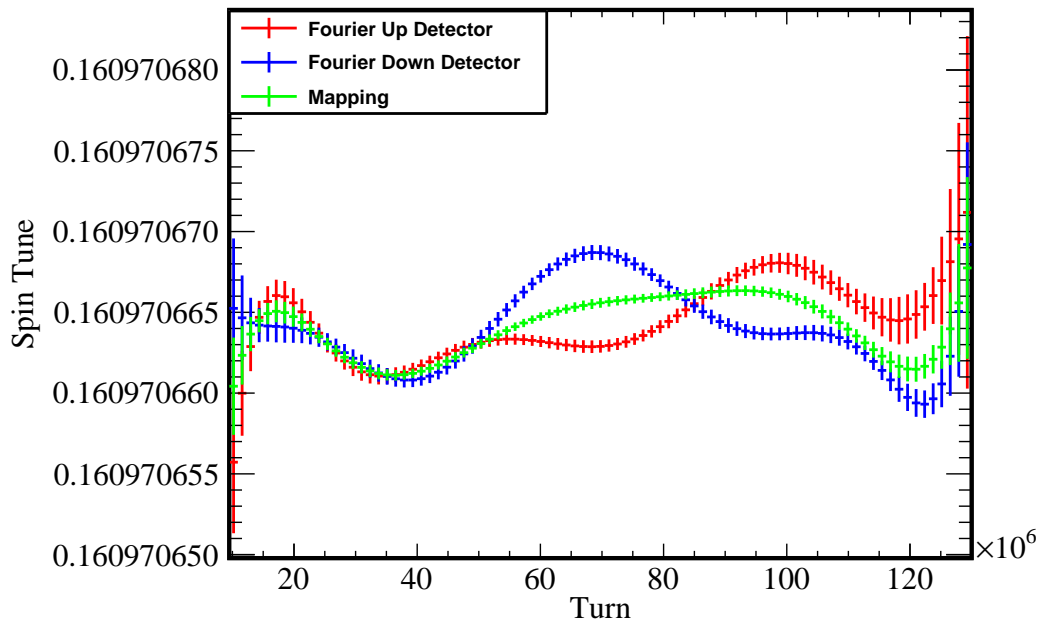


Figure 4.17.: Spin tune ν_s as a function of turns.

Wien Filter and spin tune frequency into account. Inserting the oscillating luminosity in eq. 4.3 leads to a change of the count rates in the individual detectors

$$\dot{N}_{\text{Up}} \propto (1 + a \cos(\omega_{\text{WF}}n + \varphi_{\text{WF}})) \cdot (1 - \epsilon_H \cos(\omega_s n + \varphi_s)), \quad (4.44)$$

$$\dot{N}_{\text{Down}} \propto (1 + a \cos(\omega_{\text{WF}}n + \varphi_{\text{WF}})) \cdot (1 + \epsilon_H \cos(\omega_s n + \varphi_s)), \quad (4.45)$$

$$\dot{N}_{\text{Left}} \propto (1 + a \cos(\omega_{\text{WF}}n + \varphi_{\text{WF}})) \cdot (1 + \epsilon_V), \quad (4.46)$$

$$\dot{N}_{\text{Right}} \propto (1 + a \cos(\omega_{\text{WF}}n + \varphi_{\text{WF}})) \cdot (1 - \epsilon_V), \quad (4.47)$$

with $\epsilon_V = \frac{3}{2}p_V \overline{A}_y$, $\epsilon_H = \frac{3}{2}p_{xz} \overline{A}_y$ and the dot denotes the time derivative, *i.e.* the counting rate $(\frac{dN}{dt})$.³ Note that the oscillation amplitude a is assumed to be the same in all four detectors, even though the oscillations might only occur in one plane. The beam oscillations change the count rate periodically on the target and therefore at the same time in all four detectors simultaneously.

In the following, three different scenarios are discussed. The first scenario deals with unpolarised data. The second and third scenario deal with polarised data, where the phase feedback was turned on and turned off respectively when the RF Wien Filter was switched on.

4.8.1. Unpolarised Cycles

The effect of an oscillating luminosity becomes clear when looking at unpolarised cycles, *i.e.* $p_V = p_H = 0$, reducing eq. 4.44-4.47 to

$$\dot{N}_{\text{Up}} = \alpha \overline{\sigma}_{0\text{U}} \mathcal{L}_{\text{COSY}} \cdot (1 + a \cos(\omega_{\text{WF}}n + \varphi_{\text{WF}})), \quad (4.48)$$

$$\dot{N}_{\text{Down}} = \alpha \overline{\sigma}_{0\text{D}} \mathcal{L}_{\text{COSY}} \cdot (1 + a \cos(\omega_{\text{WF}}n + \varphi_{\text{WF}})), \quad (4.49)$$

$$\dot{N}_{\text{Left}} = \alpha \overline{\sigma}_{0\text{L}} \mathcal{L}_{\text{COSY}} \cdot (1 + a \cos(\omega_{\text{WF}}n + \varphi_{\text{WF}})), \quad (4.50)$$

$$\dot{N}_{\text{Right}} = \alpha \overline{\sigma}_{0\text{R}} \mathcal{L}_{\text{COSY}} \cdot (1 + a \cos(\omega_{\text{WF}}n + \varphi_{\text{WF}})). \quad (4.51)$$

Performing a Fourier Transform of eq. 4.48 to 4.51 and normalising, results in a peak at the Wien Filter frequency ω_{WF} which corresponds to the spin tune frequency ω_s with an amplitude of a

$$A_X(\omega = \omega_{\text{WF}}) = a, \quad (4.52)$$

where $X \in \{\text{U, D, L, R}\}$ denotes the detector. In Figure 4.18 the spectra measured by the individual detectors for an unpolarised deuteron cycle using the RF Wien Filter is shown. All detectors show a clear peak when switching on the RF Wien Filter at 50×10^6 turns. The frequency of the signal is equal

³Due to visuality, the factors $\alpha \overline{\sigma}_{0X} \mathcal{L}_{\text{COSY}}$ are not displayed (with $X \in \{\text{U, D, L, R}\}$).

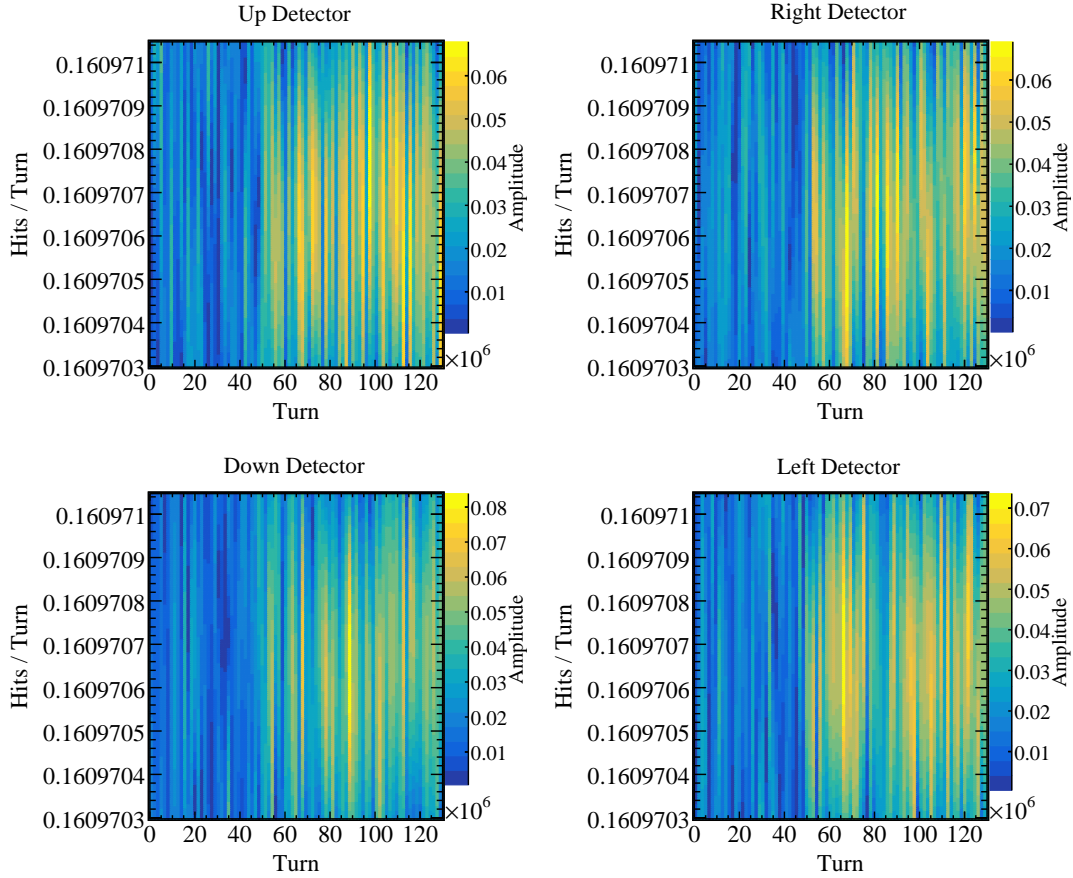


Figure 4.18.: Amplitudes measured by the individual detectors with data from an unpolarised cycle. A clear peak becomes visible at 50×10^6 turns when turning on the RF Wien Filter.

to the frequency of the spin tune even though the polarisation is zero. As expected, the amplitude measured by the individual detectors is in the same order of magnitude. In principle, the maximal amplitude of the individual spectra can be used to determine the parameter a . However, another method that is explained in section 4.8.2 is used to determine the oscillation amplitude a as in general polarised data is analysed.

4.8.2. A new Online Monitoring Luminosity Tool

The unexpected peaks in the different detectors triggered the idea of developing a new tool to monitor the periodic change of luminosity while data taking. Therefore a new program is added to the software of the DAQ of the polarime-

ter to monitor the luminosity. The idea is to monitor the Fourier amplitudes measured in the individual detectors while adjusting the electric and magnetic field inside the RF Wien Filter. When the Wien Filter is matched (Lorentz Force at the beam position is zero), the Fourier peaks due to the periodic movement of the beam are expected to vanish.

In the new online monitoring tool, all events of the individual detectors are combined, which makes it only sensitive to the luminosity change as the change of count rates due to the polarisation of the beam cancels out

$$\begin{aligned}\dot{N}_{\text{sum}} &= \dot{N}_{\text{up}} + \dot{N}_{\text{down}} + \dot{N}_{\text{left}} + \dot{N}_{\text{right}} \\ &\propto 4 + 4a \cos(\omega_{\text{WF}}n + \varphi_{\text{WF}}),\end{aligned}\tag{4.53}$$

where \dot{N} denotes the counting rate $\frac{dN}{dt}$. Performing a Fourier transform of eq. 4.53 and scaling it by the total counts measured in all four detectors $N_{\text{sum}} = N_{\text{up}} + N_{\text{down}} + N_{\text{left}} + N_{\text{right}}$ gives for the Fourier amplitude at the Wien Filter frequency

$$A_{\text{sum}}(\omega \approx \omega_{\text{WF}} = \omega_s) = a.\tag{4.54}$$

Due to the computational time, the single detector mapping method is used to calculate the sum of the signals, as it is much faster than the Fourier method because no sine or cosine functions need to be calculated.

An example of how the new monitoring will look like is shown in Figure 4.19 for a polarised cycle. The Figure in the middle shows the sum of all signals measured in the individual detectors. As soon as the RF Wien Filter is switched on, the amplitude is in the order of 0.04. For reference, the amplitudes measured by the individual detectors are also shown during a run with the phase feedback switched off, when the RF Wien Filter is turned on. The new monitoring tool allows observing the periodic change of luminosity while adjusting the electric and magnetic field inside the Wien Filter. When both fields are matched, the amplitude of the combined signals from detectors is supposed to be zero. Looking closely at the data points before the Wien Filter is switched on in Figure 4.15 - 4.17, it can be seen that results obtained with the mapping method are always in between the data points of the single detector method, even before switching on the RF Wien Filter. Additionally, also the amplitude in the middle panel in Figure 4.19 is not zero before switching on the RF Wien Filter. It is possible that the beam is periodically moving due to imperfections in the ring even before the RF Wien Filter is switched on. These systematic deviations show high sensitivity when measuring counting rates. A detailed check during the next RF Wien Filter beam time, comparing the results of the individual detectors with the combined detectors method would be interesting to do to see how well it is possible to adjust the device. In principle, it is possible to scan other periodic luminosity change, if the frequency is known and computational time allows online monitoring. However,

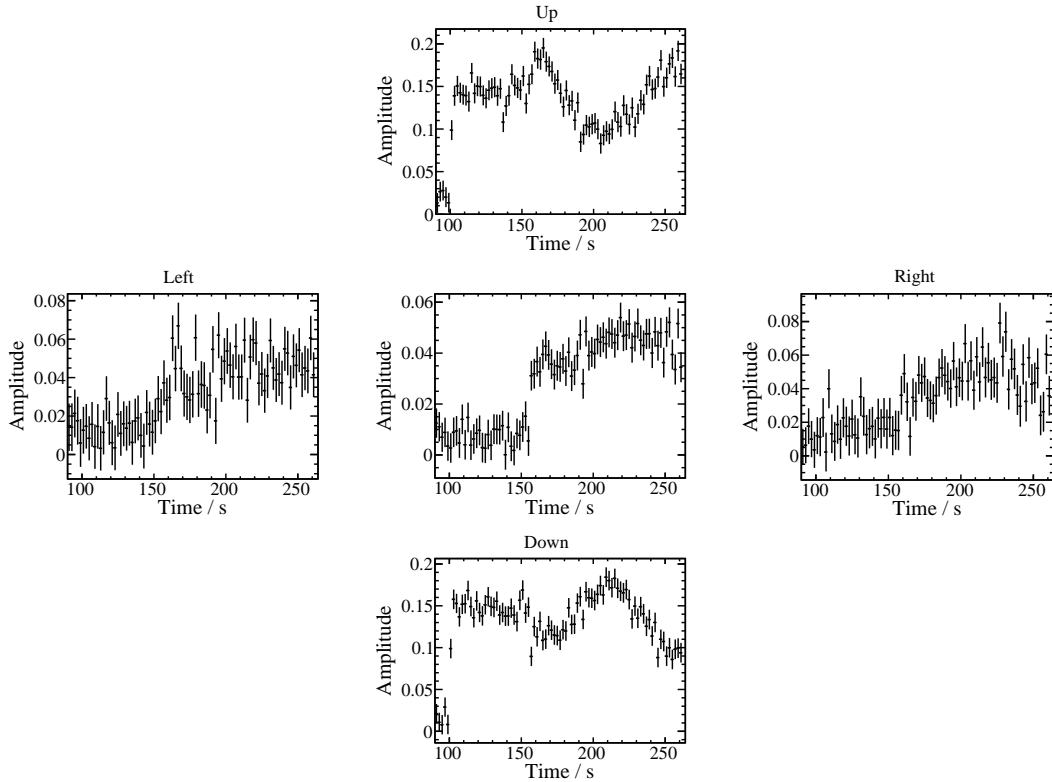


Figure 4.19.: Example of the new online luminosity monitoring tool.
Middle Panel: Sum of all four individual detectors.
Rest: Amplitudes measured by individual detectors for a polarised cycle without phase feedback when turning on the RF Wien Filter.

until now (March 2020), no Wien Filter beam time was available to test the new online tool. Note that the online monitoring only allows monitoring the beam oscillation amplitude a . A frequency and phase mismatch cannot be controlled. These parameters are adjusted with the phase feedback.

4.8.3. Cycles with Phase Feedback

In this section, data with polarised deuterons is shown. The phase feedback remains switched on when the RF Wien Filter is switched on, which means that the frequency of the Wien Filter exciting the beam is adjusted continuously with the true spin tune frequency. Additionally, the phase φ_0 between spin tune frequency and beam precession frequency remains constant, as the feedback

controls the phase between spin frequency and RF Wien Filter

$$\mathcal{L}_{\text{osc}} = \mathcal{L}_{\text{COSY}} \cdot (1 + a \cos(\omega_s n + \varphi_s + \varphi_0)). \quad (4.55)$$

The count rates in the up and down detectors are given by

$$\dot{N}_{\uparrow\downarrow} \propto (1 + a \cos(\omega_s n + \varphi_s + \varphi_0)) \cdot (1 \mp \epsilon_H \cos(\omega_s n + \varphi_s)), \quad (4.56)$$

with $\omega_s = 2\pi\nu_s$. Multiplication leads to

$$\begin{aligned} \dot{N}_{\uparrow\downarrow} \propto & 1 \mp \epsilon_H \cos(\omega_s n + \varphi_s) + a \cos(\omega_s n + \varphi_s + \varphi_0) \\ & \mp a \epsilon_H \cos(\omega_s n + \varphi_s) \cos(\omega_s n + \varphi_s + \varphi_0). \end{aligned} \quad (4.57)$$

Performing a Fourier transform leads to peaks at $\omega = 0$, $\omega = \omega_s$ and $\omega = 2 \cdot \omega_s$.⁴ Relevant is the peak at the spin tune frequency. Ignoring the other terms gives

$$\dot{N}_{\uparrow\downarrow} \propto \mp \epsilon_H \cos(\omega_s n + \varphi_s) + a \cos(\omega_s n + \varphi_s + \varphi_0). \quad (4.58)$$

The frequency of the RF Wien Filter and relative phase of the spin tune frequency and RF Wien Filter frequency are controlled and adjusted throughout the entire measuring time. As it is ensured that φ_s is adjusted, it can be set to an arbitrary value ($\varphi_s = 0$) without losing generality. For the Fourier transform only φ_0 remains relevant

$$\begin{aligned} \dot{N}_{\uparrow\downarrow} \propto & \mp \epsilon_H \cos(\omega_s n) + a \cos(\omega_s n + \varphi_0) \\ = & a (\cos(\omega_s n) \cos(\varphi_0) - \sin(\omega_s n) \sin(\varphi_0)) \mp \epsilon_H \cos(\omega_s n) \\ = & \cos(\omega_s n) \cdot (a \cos(\varphi_0) \mp \epsilon_H) + \sin(\omega_s n) \cdot (-a \sin(\varphi_0)). \end{aligned} \quad (4.59)$$

The Fourier amplitudes at the spin tune frequency are given by

$$\begin{aligned} A_{\uparrow\downarrow}(\omega = \omega_s) &= \sqrt{(a \cos(\varphi_0) \mp \epsilon_H)^2 + a^2 \sin(\varphi_0)^2} \\ &= \sqrt{a^2 + \epsilon_H^2 \mp 2a\epsilon_H \cos(\varphi_0)}. \end{aligned} \quad (4.60)$$

Amplitudes in the individual detectors depend on the horizontal polarisation ϵ_H , the beam oscillation amplitude a and the phase between beam oscillations and spin tune precession φ_0 . The phase φ_0 is a value that is fixed by the operators before starting the measurement and remains constant throughout the measuring time. In Figure 4.20 an example of a run with phase feedback switched on can be seen. The phase relation was set to $\varphi_0 = \pi$ rad. The

⁴ $\cos(a) \cos(b) = \frac{\cos(a-b) + \cos(a+b)}{2}$.

amplitudes in the individual detectors are therefore given by

$$A_{\uparrow\downarrow} = |a \pm \epsilon_H|, \quad (4.61)$$

which can be seen in Figure 4.20. A second important result is, that the measured spin tune is not affected by this effect, which can also be seen in Figure 4.20. The two detectors and the combined detector method show the same results. Small deviations can occur due to imperfections in the machine. A systematic effect could be that the beam doesn't hit the target in right angle, which would automatically increase the counting rate in a single detector, shifting the peak to higher or lower apparent spin tunes. Another effect that can occur is that the spin tune and the beam oscillation run slightly out of phase when travelling from the Wien Filter to the polarimeter. However, combining the results of the spin tunes from individual detectors leads to the same result as the combined-detector mapping method (Figure 4.22)

$$\nu_{s,\text{comb}} = \frac{\nu_{s,\uparrow} + \nu_{s,\downarrow}}{2}. \quad (4.62)$$

The amplitudes from eq. 4.61 can be used to determine the horizontal polarisation ϵ_H and the oscillation amplitude a

$$\frac{A_{\uparrow} - A_{\downarrow}}{2} = a \quad \text{and} \quad \frac{A_{\uparrow} + A_{\downarrow}}{2} = \epsilon_H. \quad (4.63)$$

The results are shown in Figure 4.21. The horizontal polarisation calculated with the combined Fourier amplitudes fits very well with the results from the mapping method. The amplitude of the beam oscillations occurs as expected when turning on the RF Wien Filter at 50×10^6 turns and is in the order of 0.04. Note that eq. 4.63 and 4.61 are only valid if the phase between spin tune frequency and Wien Filter is set to $\varphi_0 = \pi$ rad.

To confirm the equation for the amplitude of the individual detectors (eq. 4.60) a second run is analysed, where the phase relation between spin tune and Wien Filter was set to $\varphi_0 = \pi/2$ rad. The amplitudes are therefore given by

$$A_{\uparrow\downarrow} = \sqrt{a^2 + \epsilon_H^2}, \quad (4.64)$$

which means that both detectors measure the same signal despite the beam oscillations. In Figure 4.23 the results are confirmed. Plotted are the amplitudes measured by individual detectors (A_{\uparrow} and A_{\downarrow}), the beam oscillation amplitude a and the difference of the signals measured in the individual detectors. The difference is consistent with zero as a least-square fit with a polynomial of 0th order shows. The result of the fit is 0.0002 ± 0.0020 with $\chi^2/\text{ndf} = 124/86$.

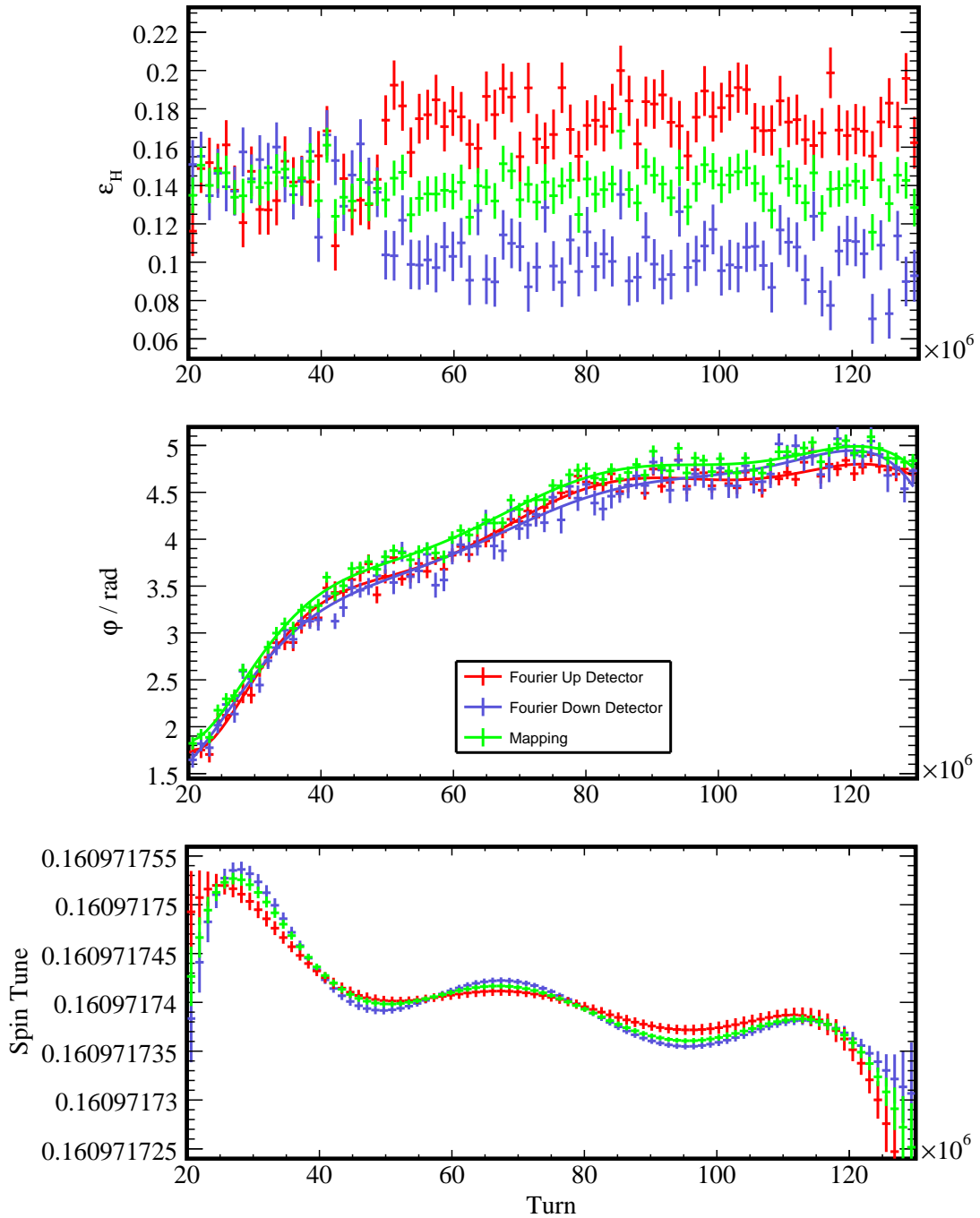


Figure 4.20.: Horizontal polarisation ϵ_H , phase φ_s and spin tune ν_s as a function of turn numbers for Run 50291 Cycle 2. While the horizontal polarisation deviates, the spin tune measured with individual detectors show the same result as the mapping method.

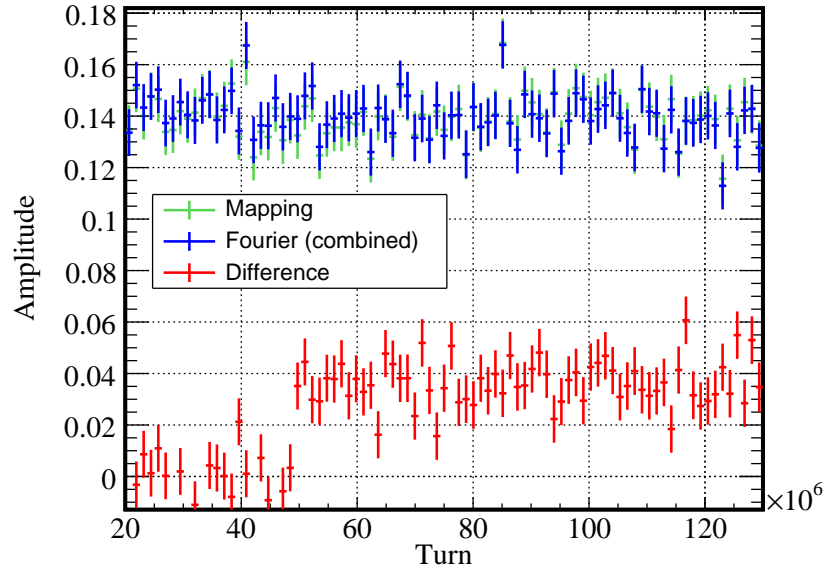


Figure 4.21.: The horizontal polarisation ϵ_H calculated with the combined-detector mapping method and the combined Fourier amplitudes. The results match within their statistical uncertainties. Additionally, the difference of the Fourier amplitudes is shown, which corresponds to the beam oscillation amplitude a and occurs when turning on the Wien Filter.

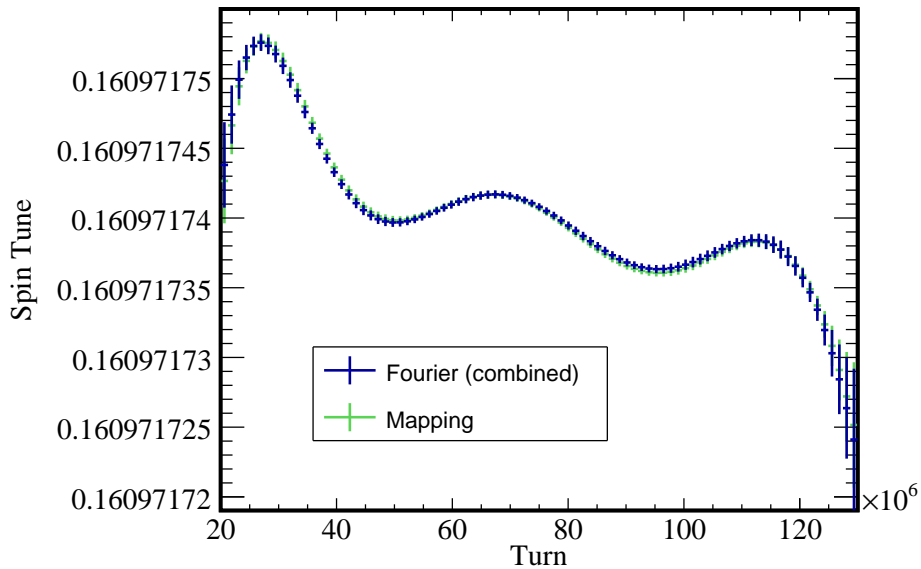


Figure 4.22.: Results of the spin tune determined with the combined-detector mapping method and the combined Fourier method.

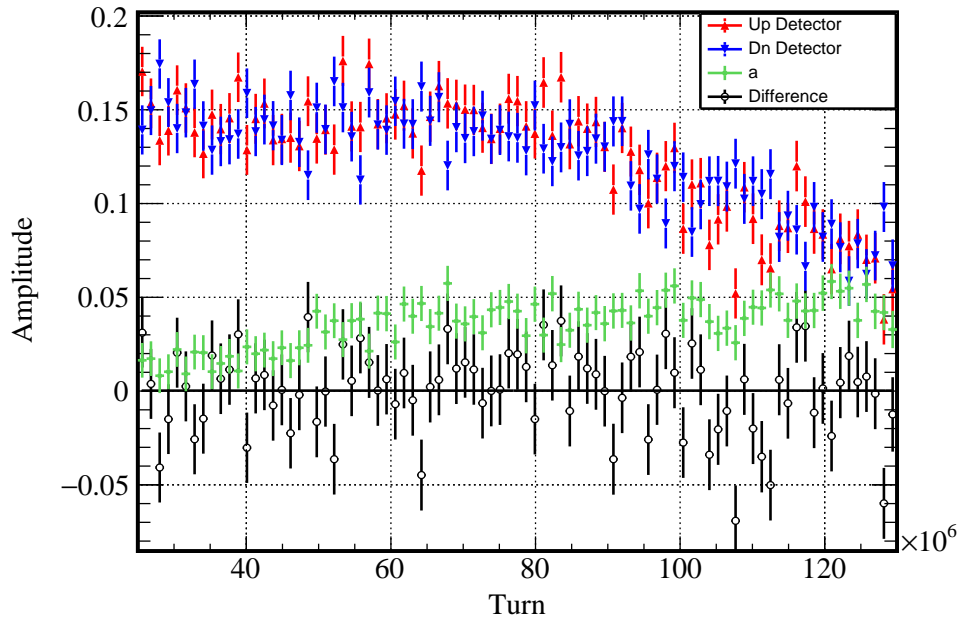


Figure 4.23.: Fourier Amplitudes measured by the individual detectors ($A_{\uparrow\downarrow}$), the amplitude of the beam oscillations a and the difference of the Fourier Amplitudes measured in the single detectors for a run, where the phase between spin tune and Wien Filter was set to $\varphi_0 = \pi/2$ rad and the phase feedback turned on when switching on the RF Wien Filter. Despite the beam oscillations, the signals in the individual detectors match as expected.

4.8.4. Cycles without Phase Feedback

In this chapter, the results shown in figure 4.15 to 4.17 is tried to be explained. However, until now this data is not understood in all details. Only an Ansatz of an analytical approach is given in this chapter to understand the behaviour. As the phase feedback is turned off, when turning on the RF Wien Filter, the equations get more complicated. The frequency ω_{WF} and the phase φ_{WF} of the Wien Filter are not adjusted by the phase feedback while measuring. These values are fixed to the frequency and phase before turning off the phase feedback. Therefore, frequency and phase remain constant with time

$$\mathcal{L}_{\text{osc}} = \mathcal{L}_{\text{COSY}} \cdot (1 + a \cos(\omega_{s,0}n + \varphi_{s,0})), \quad (4.65)$$

with $\omega_{s,0} = \omega_s(t = t_{\text{WF}})$ and $\varphi_{s,0} = \varphi_s(t = t_{\text{WF}})$. While the phase and the frequency of the Wien Filter remain constant, the spin tune and its phase change with time. The count rates in the up and down detector are given by

$$\dot{N}_{\uparrow,\downarrow} \propto (1 + a \cos(\omega_{s,0}n + \varphi_{s,0})) \cdot (1 \mp \epsilon_H \cos(\omega_s n + \varphi_s)). \quad (4.66)$$

Multiplying eq. 4.66 leads to

$$\begin{aligned} \dot{N}_{\uparrow,\downarrow} \propto 1 \mp \epsilon_H \cos(\omega_s n + \varphi_s) + a \cos(\omega_{s,0}n + \varphi_{s,0}) \\ \mp a \epsilon_H \cos(\omega_{s,0}n + \varphi_{s,0}) \cos(\omega_s n + \varphi_s). \end{aligned} \quad (4.67)$$

Performing a Fourier transform, only the terms containing the spin tune frequency are relevant, assuming that the spin tune doesn't drift too far away from the initial spin tune when turning off the phase feedback

$$\dot{N}_{\uparrow,\downarrow} \propto \mp \epsilon_H \cos(\omega_s n + \varphi_s) + a \cos(\omega_{s,0}n + \varphi_{s,0}). \quad (4.68)$$

Spin tune ω_s and phase φ_s can be replaced by

$$\omega_s = \omega_{s,0} + \Delta\omega \quad \text{and} \quad \varphi_s = \varphi_{s,0} + \Delta\varphi. \quad (4.69)$$

where $\Delta\omega$ and $\Delta\varphi$ denote the offset with respect to the spin tune and phase at the time when turning on the RF Wien Filter. Plugging into eq. 4.68 gives

$$\dot{N}_{\uparrow,\downarrow} \propto a \cos(\omega_{s,0}n + \varphi_{s,0}) \mp \epsilon_H \cos((\omega_{s,0} + \Delta\omega) \cdot n + (\varphi_{s,0} + \Delta\varphi)). \quad (4.70)$$

As only the phase relation between both oscillations is relevant, the common phase $\varphi_{s,0}$ can be set to an arbitrary value ($\varphi_{s,0} = 0$) without losing generality, reducing eq. 4.70 to

$$\dot{N}_{\uparrow,\downarrow} \propto a \cos(\omega_{s,0}n) \mp \epsilon_H \cos((\omega_{s,0} + \Delta\omega) \cdot n + \Delta\varphi). \quad (4.71)$$

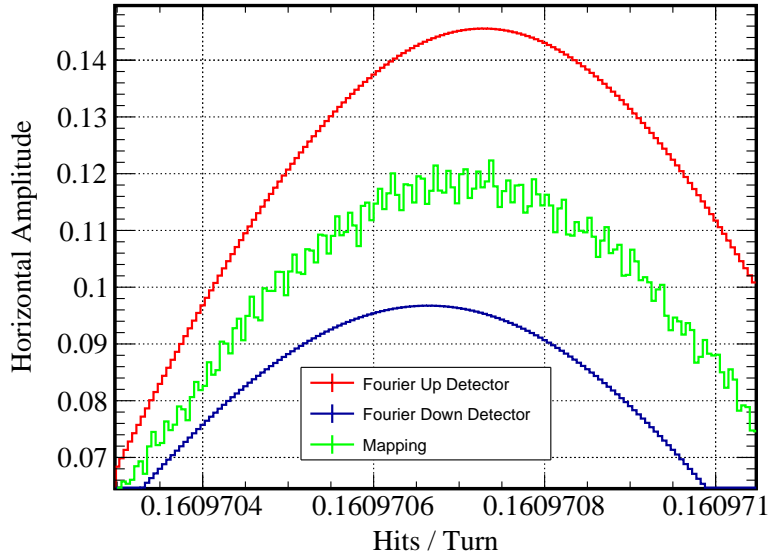


Figure 4.24.: Peaks determined by the up, down and combined detectors. All peak maxima deviate.

Mathematically, a Fourier Transform would result in two independent peaks at $\omega = \omega_{s,0}$ and $\omega = \omega_s$ with an amplitude of a and ϵ_H respectively. Due to the small drift of the spin tune $\Delta\omega$ and the smearing of the peaks, the individual peaks are not distinguishable. Only one single peak, shifted from the spin tune frequency is observable. The amplitude of the single peak is a combination of the horizontal polarisation, the beam oscillation amplitude and the time dependent phase shift between spin tune and Wien Filter. However, it was shown that the apparent spin tunes, measured by individual detectors deviate symmetrically from each other as in Figure 4.17. The reason for this behaviour is still unknown. To make it more clear, the peaks of the 43th time bin are shown in Figure 4.24. A clear displacement of all peak maxima can be seen. A second observed effect is, that the spin tune (and the peak maxima) oscillate around the combined detector method. Also the reason of this effect is still unknown. The source of this problem is probably the Wien Filter exciting the beam with a frequency that is different from the spin tune frequency as both effects are not seen in data, where the phase feedback was turned on, when turning on the Wien Filter. Also weighting the results of the spin tune measured by both single detectors from Figure 4.17 as in Figure 4.22 for the phase feedback turned on leads to nonmatching results as shown in Figure 4.25.

However, the root of this behaviour is a mismatched Wien Filter in terms of

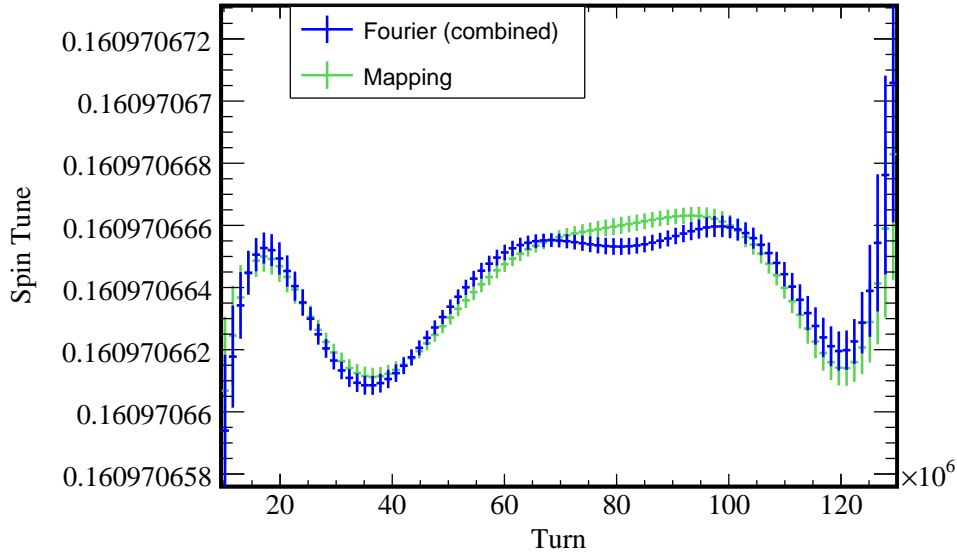


Figure 4.25.: Results of the spin tune determined with the combined-detector mapping method and the combined Fourier method for a run with phase feedback turned off.

the strengths of the electromagnetic field inside the device. The peaks seen by individual detectors are used in a new online monitoring tool to adjust the electromagnetic field by minimizing the amplitude of the oscillation a to ensure that the Lorentz force at the beam position is zero. As soon as a is minimized, the luminosity is not oscillating anymore and the frequency shift (with and without phase feedback) is not observable anymore.

For the sake of completeness, an additional cycle is shown in Figure 4.26. In this cycle the phase feedback was turned on when turning on the RF Wien Filter and set to $\varphi_0 = 3.93$ rad. The results obtained with individual detectors follow the shape of data determined with the mapping method. This may be due to the fact that the RF Wien Filter was matched better during this run and might be a promising result to make use of a new luminosity monitoring tool. However, also in this plot small deviations occur. A detailed check of the results measured by individual detectors after using the new online monitoring tool would be interesting to do.

As an additional remark, it is not recommended to use a single detector in order to determine phase φ_s , horizontal polarisation ϵ_H and spin tune ν_s and stick to the combined-detector mapping method, which is not sensitive to luminosity changes of the beam and leads to reliable results.

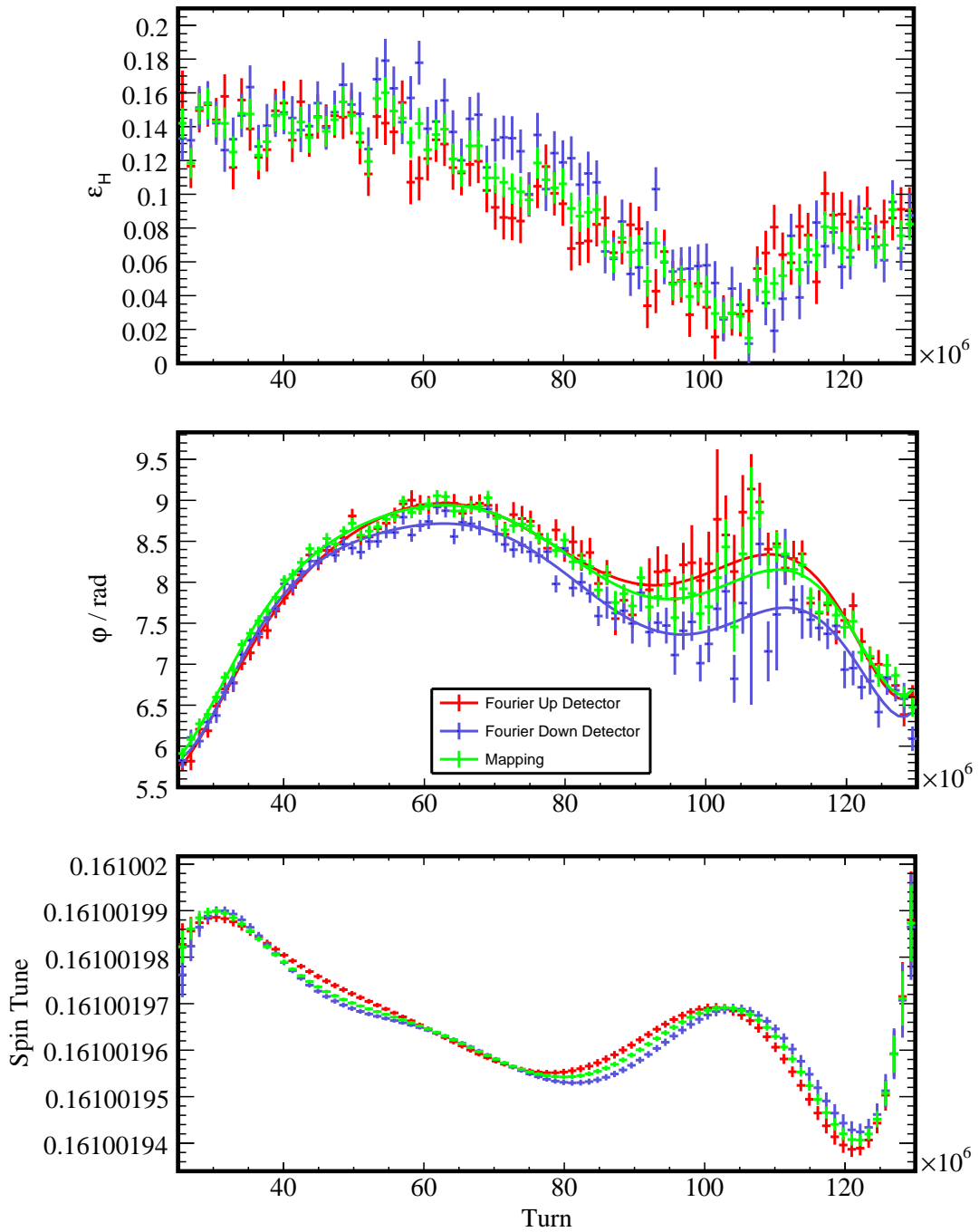


Figure 4.26.: Horizontal polarisation ϵ_H , phase φ_s and spin tune ν_s as a function of turn numbers for Run 50122 Cycle 2. Horizontal polarisation and the spin tune measured with single detectors show the same result as the mapping method.

4.9. A Detailed Spectral Analysis with Artificial Neural Networks

The unexpected peaks seen in the left and right detector due to the periodic movement of the beam triggered the idea of performing a detailed spectral scan of data to find other unexpected peaks. The idea is to scan a full frequency range. Afterwards, an artificial neural network decides whether a peak is dominant in data. In this chapter, the result of all peaks found in data is shown after a short introduction into neural networks.

4.9.1. Neural Networks - An Introduction

Machine learning is a technique in computer science to derive decision rules from data. The method used in this thesis is called supervised learning. The network is trained in an iterative process with pairs of input and desired output data. The network tries to derive rules which replicate the known output. The aim is to find rules which produce the desired output on new data. The following theory focuses on a classification task [37]. The neural networks used in this thesis are created with Keras [38] using the TensorFlow [39] backend. The basic unit of a neural network is a neuron, in analogy to a neuron in a human brain. The neuron receives inputs from other neurons as numerical values. As different inputs have different importances, each input is weighted accordingly. Afterwards, the signal is passed to an activation function $\sigma(x)$, as otherwise, the neural network would only represent a linear relationship. In many scenarios, the relationship between input and output data is nonlinear. Mathematically, the output of a neuron can be written as

$$y = \sigma \left(\sum_i w_i x_i + b \right), \quad (4.72)$$

where the inputs and the corresponding weights are given by x_i and w_i . The bias parameter of the neuron and the activation function are denoted as b and σ . The final output is y [40]. The most common used activation function, which is also used in this work (see Figure 4.27), is called rectified linear unit (ReLU) [41]

$$\text{ReLU}(x) = \max(x, 0). \quad (4.73)$$

In the context of this work, neural networks are used for a classification task, which means that the network learns pattern and classifies the data accordingly. The output of the neural network is therefore a probability value for

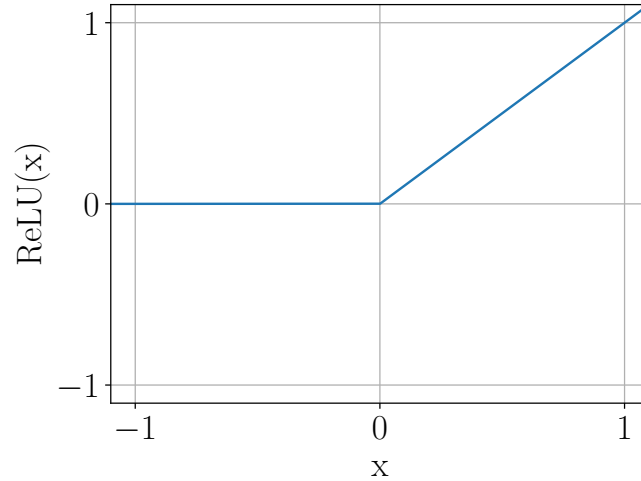


Figure 4.27.: ReLU activation function, used in this work.

each possible class with

$$\sum_i y_i = 1. \quad (4.74)$$

In general, the output range of a neural network is $(-\infty, \infty)$. An activation function that guaranties normalised probabilities in $[0, 1]$, is called softmax function

$$\sigma_i(\vec{y}) = \text{softmax}_i(\vec{y}) = \frac{e^{y_i}}{\sum_k e^{y_k}}, \quad (4.75)$$

where i denotes the output of the i -th neuron [42].

Dense/ Fully Connected Layers In neural networks, neurons are organized in layers, so that a neuron receives only inputs from neurons in the layer before and only sends outputs to neurons in the next layer. In a dense layer, each neuron receives an input from every neuron in the preceding layer (see Figure 4.28). The output of a combined dense layer can be written as

$$y_i = \sigma \left(\sum_j w_{ij} x_j + b_i \right). \quad (4.76)$$

Note that the weight w from eq. 4.72 changed into a $n_{\text{Neurons}} \times n_{\text{Inputs}}$ matrix and the bias b into a vector with the size of the number of neurons n_{Neurons} . If two or more layers are connected this way, one speaks of a neural network.

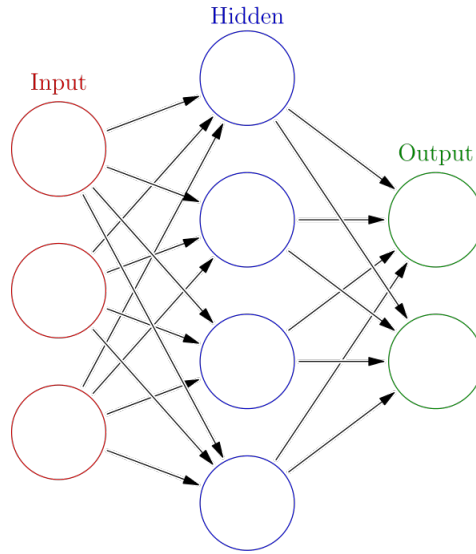


Figure 4.28.: A schematic sketch of an artificial neural network with an input layer, one hidden layer and one output layer. The arrows denote the corresponding weights [43].

The output of a neural network with multiple layers is given by

$$\begin{aligned} \text{out}_i &= \sigma \left(\sum_j w_{ij}^n x_j^{n-1} + b_i^n \right) \\ &= \sigma \left(\sum_j w_{ij}^n \sigma \left(\sum_k w_{jk}^{n-1} (\dots) + b_j^{n-1} \right) + b_i^n \right), \end{aligned} \quad (4.77)$$

where i denotes i -th output neuron and n the total number of layers. The softmax activation function is used in the last layer of the network to guaranty a normalized probability output [42].

Convolutional Layers

The basic principle of a convolutional layer consists of filters, called kernels, that have a much smaller size than the input of the data. Each kernel consists of random values. Each data point of a subsection of the full dataset is weighted. Afterwards, the weighted values are summed up and an activation function is applied. Mathematically, a convolutional layer operation can be written as

$$S(i, j) = \sum_m \sum_n I(m, n) K(i - m, j - n), \quad (4.78)$$

$$\begin{pmatrix} 0 & 1 & 1 & 1 & 0 & 0 & 0 \\ 0 & 0 & 1 & 1 & 1 & 0 & 0 \\ 0 & 0 & 0 & 1 & 1 & 1 & 0 \\ 0 & 0 & 0 & 1 & 1 & 0 & 0 \\ 0 & 0 & 1 & 1 & 0 & 0 & 0 \\ 0 & 1 & 1 & 0 & 0 & 0 & 0 \\ 1 & 1 & 0 & 0 & 0 & 0 & 0 \end{pmatrix} * \begin{pmatrix} 1 & 0 & 1 \\ 0 & 1 & 0 \\ 1 & 0 & 1 \end{pmatrix} = \begin{pmatrix} 1 & 4 & 3 & 4 & 1 \\ 1 & 2 & 4 & 3 & 3 \\ 1 & 2 & 3 & 4 & 1 \\ 1 & 3 & 3 & 1 & 1 \\ 3 & 3 & 1 & 1 & 0 \end{pmatrix}$$

Figure 4.29.: Convolutional Layers: The matrices from left to right denote the input data matrix I , kernel K and feature map S [45].

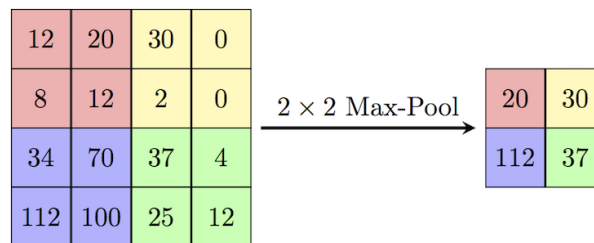


Figure 4.30.: Schematic principle of Max Pooling Layers. The data input is divided in subsets, where only the maximum of the subset is passed to the next layer of the network architecture [47].

where I denotes a two-dimensional input data image and K a two-dimensional kernel. The result S is called feature map. The values of K are trainable weights and the same for every segment of I .

The principle is shown in Figure 4.29. The big matrix on the left shows arbitrary data and the marked red box denotes the segment on which the kernel is applied. Each data point is multiplied with the corresponding weight of the kernel. The last matrix shows the summation of all values. It is obvious, that a convolutional layer drastically reduces the size of input data (and so the training time) which is useful for high input dimensions [44].

Max Pooling Layers

A more efficient way to reduce the size of input data, is using so-called Max Pooling Layers, where only the maximum of a subset of the full data range is passed to the next layer. The pooling size and the stride denote the dimension of the image section, where the pooling is applied and the number of data points the pooling filter is moved for the next pooling step. The principle is shown in Figure 4.30. In neural networks, it is common that convolutional layers and max pooling layers are used in multiple pairs [46].

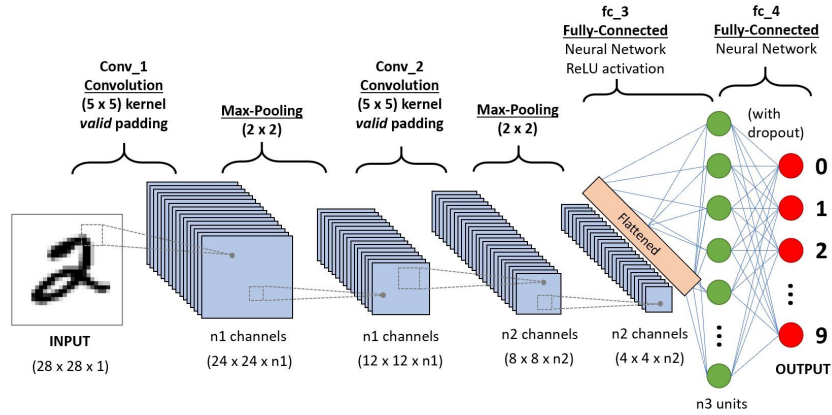


Figure 4.31.: An example of a full architecture of an neural network. From left to right: Input Data, Alternating Convolutional and Max Pooling Layers, Flattening, Dense Layers and the final output. A similar architecture is used in this work, see section 4.9.3 [48].

A Full Architecture

In Figure 4.31 an example of a full neural network architecture is shown. Starting from the input data, alternating convolutional and max pooling layer filter more and more features in data while reducing the dimension. Afterwards a flatten layer is applied, which transforms the matrix into a one-dimensional array, which is used as an input for the classification task, done by a series of dense layers. The output is in this case a 9 dimensional vector output for the numbers between 1 and 9. A similar architecture is also used in this thesis.

4.9.2. Generation of Data

The dataset is generated with the Fourier method as described in chapter 4.5. Until now, a frequency range from 0 kHz to 150 kHz and 350 kHz to 500 kHz is scanned in all four detectors simultaneously for a polarised and unpolarised dataset. The network is trained with spectra having 20 bins in time from 0 to 130×10^6 turns and 150 bins in the frequency domain with a frequency range of $\Delta f = 3.75$ Hz. Therefore the entire dataset is after being analysed split into frequency ranges of 3.75 Hz and predicted by the network. Some examples of a few spectra generated this way are shown in Figure 4.32.

4.9.3. Network Training

For a neural network, the number of free parameters (weights) can be huge. Their determination is automatized during the so-called training process. A loss

function is the target function of the optimization performed while training a neural network. It quantifies how close the reconstructed output \hat{y} is to the true output y . The aim of the neural network is to minimize the loss function. In this thesis the so-called categorical cross entropy is used as a loss function

$$\text{Cross Entropy} = -\frac{1}{N_{\text{samples}}} \sum_{N_{\text{samples}}} \sum_i^{\# \text{ nodes}} s_i^{\text{true.}} \ln \left(s_i^{\text{pred.}} \right), \quad (4.79)$$

where s_i is the softmax output of the i -th neuron [49]. The training of a neural network is conducted in several iterations, so-called epochs. Before the first epoch starts, all parameters are set to random values. In each epoch, the loss function and the reconstructed output are generated. The weights and biases of the network are optimized each epoch by the stochastic gradient descent

$$\vec{w}' = \vec{w} - \alpha \nabla L(\vec{w}), \quad (4.80)$$

where \vec{w} denotes a vector containing the weights and the learning rate α determines the stepsize [50]. In principle, it is possible to reach the local minimum of the loss function. However, efficient optimizers like Adam [51] that adaptively adjust the learning rate are commonly used. Before training the neural network, the labeled dataset is divided into a training and a validation data sample. During training, the network only uses the training data sample. The validation dataset is evaluated with the trained model after each epoch to ensure that the network learns the structure of data, rather than memorizing the training data (overtraining). A second intuitive indicator of the performance of the neural network is the accuracy

$$\text{acc} = \frac{\# \text{Correct Predictions}}{N_{\text{Data}}}. \quad (4.81)$$

The output gives the percentage of correctly predicted data. For the training process, in total 300 spectra are used, 150 of them containing a peak and 150 not. An example set of training data can be seen in Figure 4.32. The first column shows three clear peaks, while the second column contains only data with noise. The network is trained for 1000 epochs. The final architecture of the neural network containing more details is shown in Figure 4.34. The performance of the network can be seen in Figure 4.33. The accuracy of the network quickly reaches 100%, while the loss decreases continuously when training the network during the epochs, which means that the efficiency of the network differentiating dominant peaks and noise for the training and validation set increases. The threshold for the probability of detecting a peak is given by $p_{\text{Peak}} > p_{\text{NoPeak}}$, *i.e.* $p_{\text{Peak}} > 0.5$.

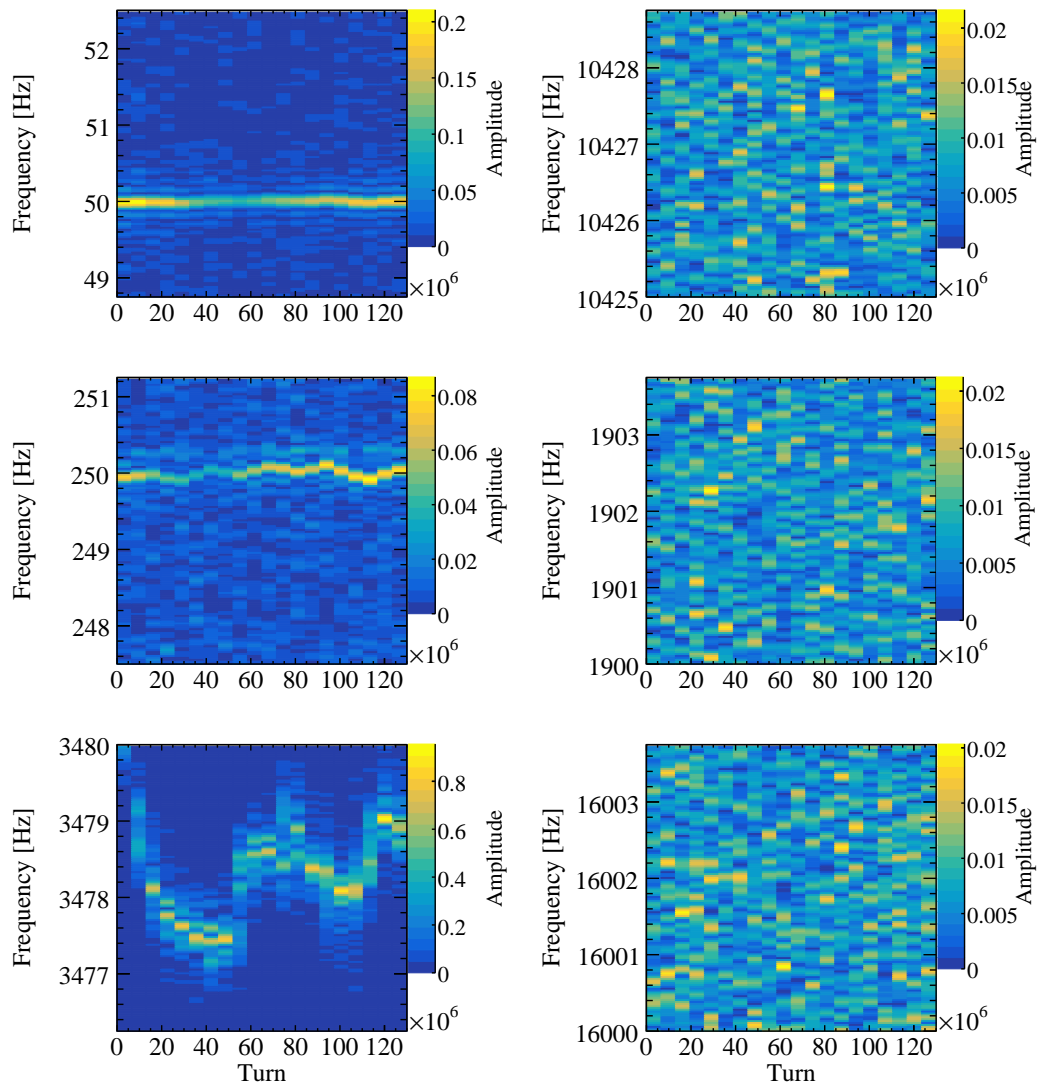


Figure 4.32.: Examples of data that is used to train the network. The first column shows three spectra with a dominant peak. The second column contains spectra which show noise.

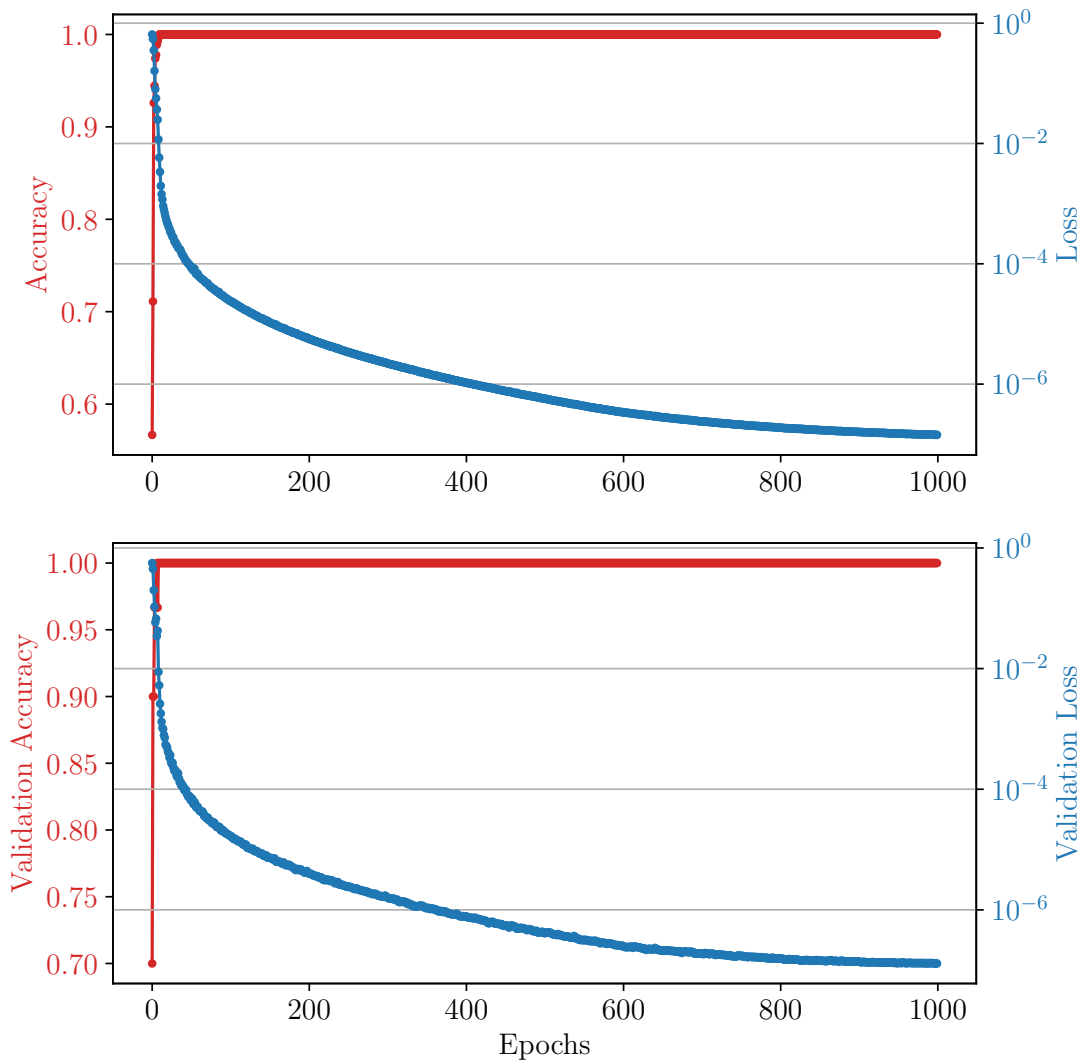


Figure 4.33.: a) Accuracy and Loss b) Validation Accuracy and Validation Loss, when training on the real data training set. The accuracy reaches in both cases 100%, which means that all peaks of the training and validation set are correctly identified.

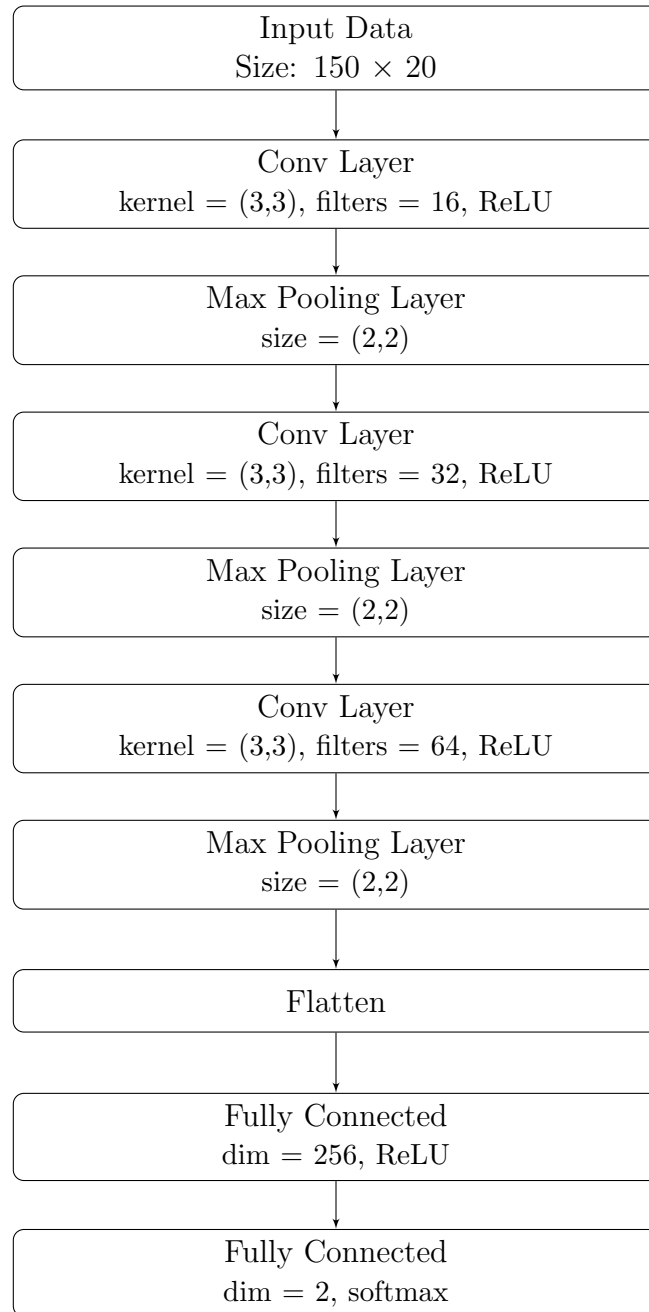


Figure 4.34.: Network Architecture: The spectra are used as an input for alternating convolutional and max pooling layers, followed by two fully connected layers, performing the binary classification task.

4.9.4. Results

In total 869 peaks are found in polarised data and 959 peaks are found in unpolarised data in a frequency range from 0 Hz to 150 000 Hz and 350 000 Hz to 500 000 Hz. Peaks appear in the frequency range from 0 Hz to 11 000 Hz (Fig. 4.35), 115 845 Hz to 125 801 Hz (Fig. 4.36) and 465 285 Hz to 472 833 Hz (Fig. 4.37). Due to the high amount of peaks, it is not possible to discuss each peak in detail. However, a more general approach, trying to understand structures and dominant peaks are given in the following, even though the source of most detected peaks can only be guessed.

Figure 4.35 to 4.37 have the same structure. The first plot shows the probability of the network detecting a peak as a function of frequency and detector (red labels: polarised and blue labels: unpolarised). If the network detects a peak, a coarse amplitude scan is performed. Assuming that a peak has the highest amplitude of a scanned spectra in a 3.75 Hz frequency interval, all amplitudes in a full time spectra (20) are collected. The second plot shows the absolute maximal amplitude of the corresponding spectra and the third Figure the lowest peak maxima. This procedure gives a rough estimation of the dynamic of the peak amplitude and is not a precise tool to determine amplitudes. A more precise method would be to fit each peak by a gaussian and determine the amplitude with a fit parameter, which would go beyond the scope of this analysis.

In Figure 4.35 the detected peaks in a low frequency range from 3.75 Hz to 11 000 Hz are shown. Most of the peaks appear in a low frequency range from 3.75 Hz to 1800 Hz and around 3500 Hz. The x -axis range doesn't start from zero because the amplitude of the 0 Hz peaks would suppress the amplitude axis in the second plot, as the amplitude is 2, which becomes obvious by plugging in $\nu_s = 0$ in eq. 4.29 and 4.30. In the first range a dominant peak is for example at 50 Hz, which also corresponds to the frequency of the European AC voltage (see also Figure 4.32 first column, first plot). A lot of peaks appear at even multiples of 50 Hz. The highest peak in the first range appears at 300 Hz with a maximum amplitude of 0.6. At 3500 Hz a second peak with a high amplitude of 0.9 appears, which is also shown in Figure 4.32. Note that this amplitude is higher by a factor of 4, compared to the amplitude of the frequency, which corresponds to the true spin tune. A lot of peaks are distributed symmetrically around this peak. They all share the same structure of the main peak, but with lower amplitude. The reason for this peak is unknown. In general, no noticeable difference between polarised and unpolarised data is observed.

In Figure 4.36, the detected peaks in a range around the spin tune are shown. At roughly 120 800 Hz, the spin tune frequency can be seen, with the cor-

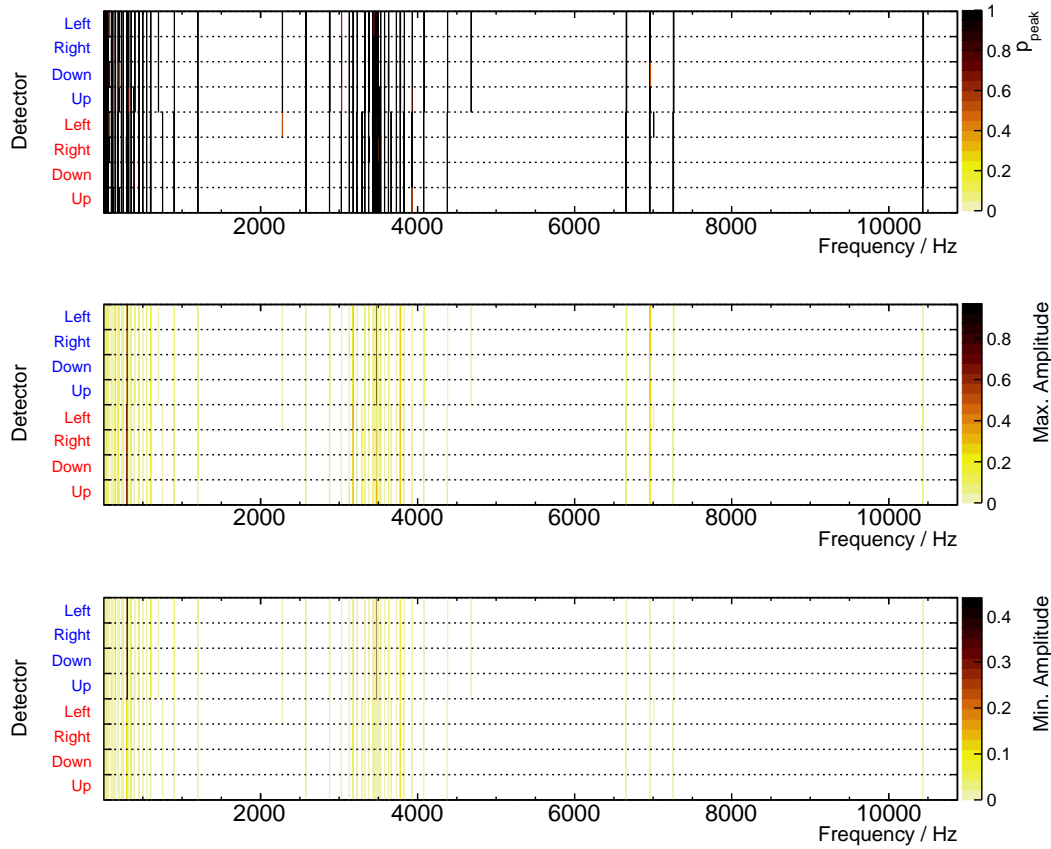


Figure 4.35.: Peaks detected by the neural network in a frequency range from 3.75 Hz to 11 000 Hz. The first plot shows the probability of a peak given by the neural network as a function of frequency and detector. The second plot shows the maximal and the third plot the minimal amplitude of corresponding spectra. The red detector labels denote the peaks measured with a polarised and the blue labels with an unpolarised beam.

responding peaks in the left and right detectors and the peaks seen in the unpolarised data, caused by the RF Wien Filter exciting beam oscillations. As expected, the amplitudes in the up and down detector show the highest amplitude due to the spin precession, which is in the order of 0.2. The other detectors show the amplitude of the periodic beam motion, which is in the order of 0.04. Additionally, four more peaks, symmetrically distributed around the spin tune (two on each side) with much less amplitude, are observed. They only occur in the up and down detector, as it is expected only for the spin tune frequency with an unperturbed beam.

The last set of peaks is found in a very high-frequency range of 465 285 Hz to

4.9. A DETAILED SPECTRAL ANALYSIS WITH ARTIFICIAL NEURAL NETWORKS

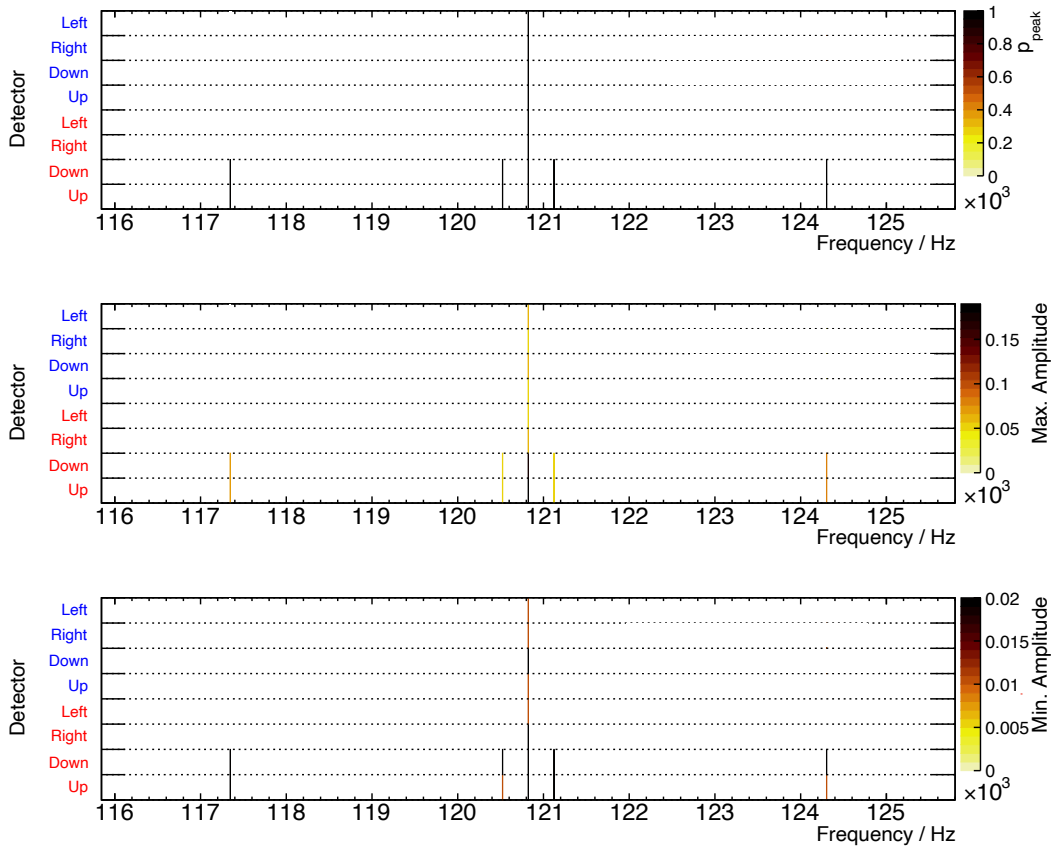


Figure 4.36.: Peaks detected by the neural network in a frequency range from 115 845 Hz to 125 801.25 Hz. The first plot shows the probability of a peak given by the neural network as a function of frequency and detector. The second plot shows the maximal and the third plot the minimal amplitude of corresponding spectra. The red detector labels denote the peaks measured with a polarised and the blue labels with an unpolarised beam.

472 833.75 Hz. In this region, most of the peaks are found, while in unpolarised data much more peaks appear. Most of the peaks have a small amplitude in the order of 0.03. However, some peaks, especially in unpolarised data, have an amplitude of 0.15, which is comparable to the amplitude of the spin tune frequency. Around 469 000 Hz, a lot of very dense peaks appear with small amplitudes of 0.03.

Until now, these are all peaks, that are found in two data sets. Most of these peaks are unexpected and might be sources of new systematic imperfections

4.9. A DETAILED SPECTRAL ANALYSIS WITH ARTIFICIAL NEURAL NETWORKS

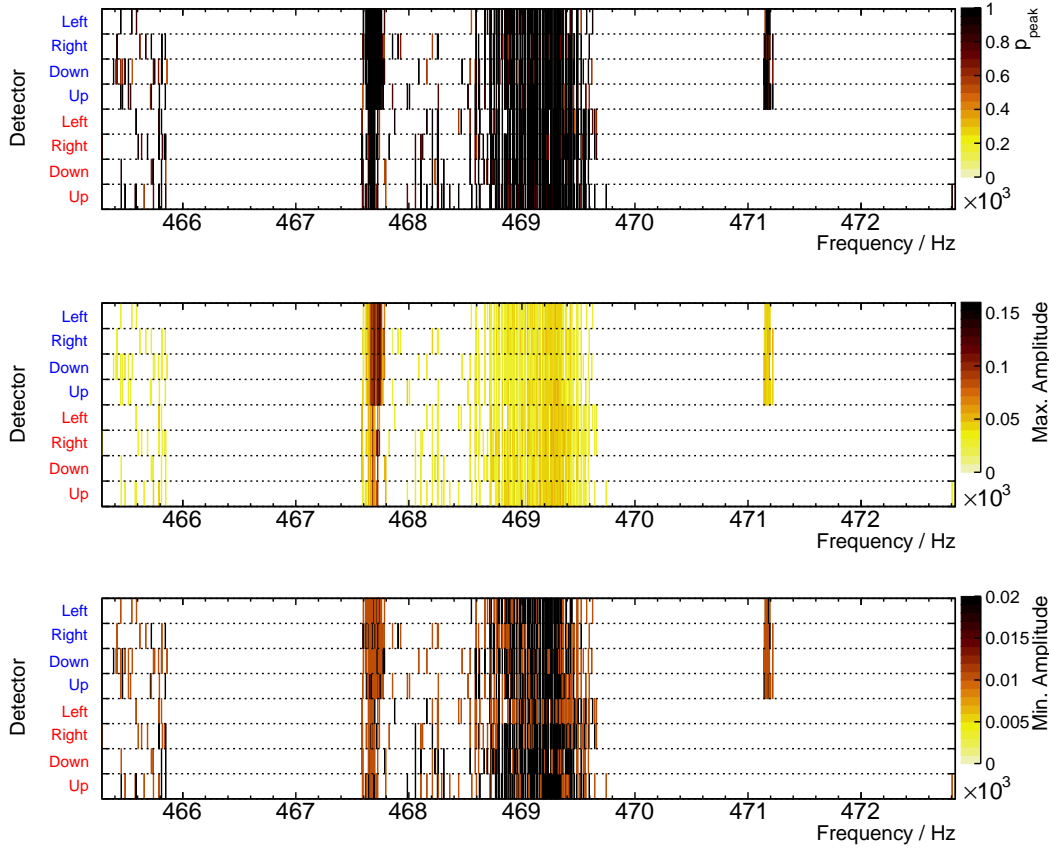


Figure 4.37.: Peaks detected by the neural network in a frequency range from 465 285 Hz to 472 833.75 Hz. The first plot shows the probability of a peak given by the neural network as a function of frequency and detector. The second plot shows the maximal and the third plot the minimal amplitude of corresponding spectra. The red detector labels denote the peaks measured with a polarised and the blue labels with an unpolarised beam.

in the machine. These peaks occur probably due to various reasons, regarding the beam and the detector itself. In principle devices like vacuum pumps, dark currents etc. can cause peaks.

However, it would be particularly interesting to investigate the peak 3500 Hz, as its amplitude is greater than the amplitude of any other peak. Due to computational time, it was not possible to scan more datasets on a full frequency range to compare peaks found in this data with old data or new data. Especially a comparison to data taken with the new polarimeter JePo installed in November 2019 in COSY would be very interesting to do in near future.

5. Conclusion

The JEDI collaboration at Forschungszentrum Jülich, Germany aims to directly measure the electric dipole moment (EDM) of charged elementary particles like protons and deuterons for the first time with the existing storage ring COSY during the so-called precursor experiment. Horizontally polarised particles in a magnetic ring precess around the vertical axis with the so-called spin tune frequency. Therefore the horizontal polarisation vector points 50% of the measuring time parallel and 50% antiparallel to the beam motion. Mathematically, it can be shown that the EDM induces an oscillating vertical polarisation due to the spin precession. However, the amplitude of this oscillation is too small to be detected directly. Therefore a novel RF Wien Filter was built, which has a electric and magnetic field perpendicular to each other and the beam direction. At the desired momentum, the particles are not affected by the field, which makes the device an ideal polarisation manipulator. Each time the beam enters the device, the magnetic field gives a kick to the polarisation precession, breaking the symmetry between parallel and antiparallel beam motion, which leads to a measurable vertical polarisation net signal. However, also systematic effects like misaligned magnets in the ring can induce a vertical polarisation buildup of the beam, independent from the electric dipole moment. A big challenge is to reduce systematic effects to their absolute minimum. The polarisation is measured with a polarimeter: Particles hit a target and scatter, depending on their polarisation, into four different segments of a detector called up, down, left and right detector as seen from the beam.

In this work, the analysis of data taken during the first precursor run in November 2018 is presented. A focus of analysis is set to the results measured by single detectors. Mathematically, the up and down detector should measure the same phase φ_s , horizontal polarisation ϵ_H and spin tune ν_s as a function of time. However, a striking deviation occurs in the single detectors, as soon as the RF Wien Filter is switched on. These deviations are caused by a misaligned electromagnetic field inside the RF Wien Filter. Everytime the device rotates the polarisation precession vector, it can also excite unintended beam oscillations if the Lorentz force at the beam position is not zero. These beam oscillations are observable as luminosity changes in the WASA polarimeter. As the change of luminosity is periodic with the same frequency as the Wien Filter Frequency, performing a Fourier transform of the counting rates in the

detectors leads to peaks at the spin tune frequency. A new program is added to the DAQ of the detector, to monitor periodic rate changes in a frequency range around the spin tune frequency while data taking, as the beam oscillation frequency is expected to have the same frequency as the spin tune. This new monitoring system can be used to adjust the electromagnetic radio frequency field inside the RF Wien Filter to ensure stable working conditions and reduce systematic errors during the next precursor run of the EDM project. The program will be tested during the next RF Wien Filter beam time at COSY.

As an additional remark, it is not recommended to use a single detector in order to determine phase φ_s , horizontal polarisation ϵ_H and spin tune ν_s and stick to the combined-detector mapping method [36], which is not sensitive to luminosity changes of the beam and leads to reliable results.

Periodic beam oscillations are one of many sources to cause signals in the polarimeter. In the last part of this work, a detailed spectral analysis of signals measured in the individual detectors is done with artificial neural networks. A large frequency range is scanned. Afterwards an artificial neural networks decides whether a dominant peak is present in data. In total almost 2000 peaks are found in an polarised and unpolarised dataset, of which origins are mostly unknown. In the future, further investigations should be carried out in order to investigate especially peaks with high amplitude.

A. Fourier Method - Calculations

A.1. Fourier Parameters Error

In this chapter, a detailed derivation of the statistical errors of the Fourier parameters (eq. 4.31 and 4.32), is given. Assuming an arbitrary function $f(x)$, where the variable x is distributed according to a probability density function n with $\langle N \rangle = \int n(x)dx$. The expectation value of f is given by

$$\langle f \rangle = \frac{\int f(x)n(x)dx}{\int n(x)dx} = \frac{1}{\langle N \rangle} \int f(x)n(x)dx. \quad (\text{A.1})$$

Taking discrete values of x_i yields

$$\sum f_i \approx \int f(x)n(x)dx. \quad (\text{A.2})$$

Plugging eq. A.2 into eq. A.1 gives

$$\langle f \rangle = \frac{\sum f_i}{\langle N \rangle} \Leftrightarrow \langle f \rangle \langle N \rangle = \sum f_i. \quad (\text{A.3})$$

Assuming statistical independence between f and n , the expectation value of $\sum f_i$ can be written as

$$\left\langle \sum f_i \right\rangle = \langle \langle f \rangle \langle N \rangle \rangle = \langle f \rangle \langle N \rangle. \quad (\text{A.4})$$

The covariance of two statistically independent functions f and g , distributed according to a common probability function n is given by

$$\begin{aligned} \text{Cov} \left(\sum f_i, \sum g_i \right) &= \left\langle \left(\sum f_i \right) \left(\sum g_i \right) \right\rangle - \left\langle \sum f_i \right\rangle \left\langle \sum g_i \right\rangle \\ &= \left\langle \sum_{i=j} f_i \cdot g_j + \sum_{i \neq j} f_i \cdot g_j \right\rangle - \langle N \rangle^2 \langle f \rangle \langle g \rangle \\ &= \langle N \rangle \langle fg \rangle + (\langle N(N-1) \rangle) \langle f \rangle \langle g \rangle - \langle N \rangle^2 \langle f \rangle \langle g \rangle \\ &= \langle N \rangle \langle fg \rangle + (\langle N^2 \rangle - \langle N \rangle^2) \langle f \rangle \langle g \rangle \end{aligned} \quad (\text{A.5})$$

Assuming N to be poisson distributed, leads to

$$\langle N^2 \rangle - \langle N \rangle^2 = \langle N \rangle. \quad (\text{A.6})$$

Therefore, eq. A.5 reduces to

$$\text{Cov} \left(\sum f_i, \sum g_i \right) = \langle N \rangle \langle fg \rangle = \sum f_i \cdot g_i. \quad (\text{A.7})$$

By choosing $f = g$, the statistical error of a weighted sum is given by [52]

$$\sigma^2 \left(\sum f_i \right) = \text{Cov} \left(\sum f_i, \sum f_i \right) = \sum f_i^2. \quad (\text{A.8})$$

A.2. Fourier Amplitudes without luminosity effects

The count rates in the four different detectors are given by

$$\frac{dN_{\text{Up}}}{dt} = \mathcal{L} \cdot \alpha \cdot \bar{\sigma}_0 \cdot \left(1 - \frac{3}{2} P_H \bar{A}_y \right), \quad (\text{A.9})$$

$$= \mathcal{L} \cdot \alpha \cdot \bar{\sigma}_0 \cdot \left(1 - \frac{3}{2} P_{xz} \bar{A}_y \sin(2\pi\nu_s f_{\text{rev}} t + \varphi_s) \right), \quad (\text{A.10})$$

$$\frac{dN_{\text{Down}}}{dt} = \mathcal{L} \cdot \alpha \cdot \bar{\sigma}_0 \cdot \left(1 + \frac{3}{2} P_H \bar{A}_y \right) \quad (\text{A.11})$$

$$= \mathcal{L} \cdot \alpha \cdot \bar{\sigma}_0 \cdot \left(1 + \frac{3}{2} P_{xz} \bar{A}_y \sin(2\pi\nu_s f_{\text{rev}} t + \varphi_s) \right). \quad (\text{A.12})$$

Performing a Fourier transform in the spin tune domain ($f_{\text{rev}} = 1$) leads to an estimate of the amplitude measured in the up and down detector

$$F(\nu)_{\uparrow\downarrow} = \int_{-\infty}^{\infty} \frac{dN_{\uparrow\downarrow}}{dt} e^{-2\pi i \nu t} dt \quad (\text{A.13})$$

$$= \frac{1}{2} \mathcal{L} \cdot \alpha \cdot \bar{\sigma}_0 \left(\pm \epsilon_H e^{i\varphi_s} \delta(\nu_s - \nu) \mp \epsilon_H e^{-i\varphi_s} \delta(\nu_s + \nu) + 2\delta(\nu) \right) \quad (\text{A.14})$$

where δ denotes the delta distribution. Additionally $\epsilon_H = \frac{3}{2} P_{xz} \bar{A}_y$ is introduced. Note that usually in signal processing, the prefactor $1/\sqrt{2\pi}$ is ignored for the Fourier transform. It is introduced for the reverse transformation

A.2. FOURIER AMPLITUDES WITHOUT LUMINOSITY EFFECTS

$$(\mathcal{F}f)(y) = \int_{\mathbb{R}^n} f(x) e^{-2\pi i y \cdot x} dx \quad (\text{A.15})$$

$$f(x) = \frac{1}{(2\pi)^n} \int_{\mathbb{R}^n} (\mathcal{F}f)(y) e^{2\pi i y \cdot x} dy. \quad (\text{A.16})$$

This way, the normalization based on Parseval doesn't hold anymore, which is compensated by the factor of 2 introduced in equation 4.29 and 4.30. Therefore eq. A.14 needs to be scaled by 2

$$F(\nu)_{\uparrow\downarrow} = \mathcal{L} \cdot \alpha \cdot \bar{\sigma}_0 \left(\pm \epsilon_H i e^{i\varphi_s} \delta(\nu_s - \nu) \mp \epsilon_H i e^{-i\varphi_s} \delta(\nu_s + \nu) + 2\delta(\nu) \right). \quad (\text{A.17})$$

Normalizing the Fourier amplitudes with the total number of events, measured in the individual detectors and using

$$A_{\uparrow,\downarrow}(\nu = \nu_s) = \sqrt{\text{Re}(F(\nu)_{\uparrow\downarrow})^2 + \text{Im}(F(\nu)_{\uparrow\downarrow})^2}, \quad (\text{A.18})$$

leads to

$$A_{\uparrow,\downarrow}(\nu = \nu_s) = \epsilon_H. \quad (\text{A.19})$$

Bibliography

- [1] L. Canetti, M. Drewes, and M. Shaposhnikov, *Matter and antimatter in the universe*, New Journal of Physics, 14 (2012), p. 095012.
- [2] W. Bernreuther, *CP Violation and Baryogenesis*, 2002.
- [3] A. D. Sakharov, *Violation of CP Invariance, C asymmetry, and baryon asymmetry of the universe*, Pisma Zh. Eksp. Teor. Fiz., 5 (1967), pp. 32–35.
- [4] A. Alavi-Harati *et al.*, *Observation of direct CP Violation in $K_{S,L} \rightarrow \pi\pi$ decays*, Phys. Rev. Lett., 83 (1999), pp. 22–27.
- [5] B. Aubert *et al.*, *Direct CP Violating Asymmetry in $B_0 \rightarrow K + \pi^-$ Decays*, Physical Review Letters, 93 (2004).
- [6] I. B. Khriplovich and S. K. Lamoreaux, *CP violation without strangeness: Electric dipole moments of particles, atoms, and molecules*, 1997.
- [7] *JEDI Collaboration*. <http://collaborations.fz-juelich.de/ikp/jedi/>, 2020.
- [8] V. Bargmann, L. Michel, and V. L. Telegdi, *Precession of the Polarization of Particles Moving in a Homogeneous Electromagnetic Field*, Phys. Rev. Lett., 2 (1959), pp. 435–436.
- [9] J. Slim, *A Novel Waveguide RF Wien Filter for Electric Dipole Moment Measurements of Deuterons and Protons at the COoler SYNchrotron (COSY)/Jülich*, PhD thesis, RWTH Aachen University, 2018.
- [10] W. M. Morse, Y. F. Orlov, and Y. K. Semertzidis, *rf Wien filter in an electric dipole moment storage ring: The “partially frozen spin” effect*, Phys. Rev. ST Accel. Beams, 16 (2013), p. 114001.
- [11] N. Hempelmann *et al.*, *Phase Locking the Spin Precession in a Storage Ring*, Physical Review Letters, 119 (2017).
- [12] S. Karshenboim and V. Ivanov, *The g factor of the proton*, Physics Letters B, 566 (2003), p. 27–34.

-
- [13] H. Masui and M. Kimura, *Deuteron-like neutron–proton correlation in ^{18}F studied with the cluster-orbital shell model approach*, Progress of Theoretical and Experimental Physics, 2016 (2016). 053D01.
- [14] V. Anastassopoulos, *A storage ring experiment to detect a proton electric dipole moment*, Review of Scientific Instruments, 87 (2016), p. 115116.
- [15] J. Pretz, *Measurement of permanent electric dipole moments of charged hadrons in storage rings*, Hyperfine Interactions, 119 (2013).
- [16] R. Weidmann *et al.*, *The polarized ion source for COSY*, Review of Scientific Instruments, 67 (1996), pp. 1357 – 1358.
- [17] D. e. a. Chiladze, *Determination of deuteron beam polarizations at COSY*, PHYS REV SPEC TOP-AC, 9 (2006).
- [18] N. Hempelmann, *Polarization Measurement and Manipulation for Electric Dipole Moment Measurements in Storage Rings*, PhD thesis, RWTH Aachen University, 2018.
- [19] H. J. S. et al., *Current Status of the COSY Electron Cooler (Jülich, Germany)*, Atomic Energy, 94 (2003).
- [20] U. e. a. Bechstedt, *Field Measurement of the Magnets for COSY - Jülich*, (1992).
- [21] D. Prasuhn *et al.*, *Electron and stochastic cooling at COSY*, Nuclear Instruments and Methods in Physics Research Section A: Accelerators, Spectrometers, Detectors and Associated Equipment, 441 (2000), pp. 167 – 174.
- [22] A. Lehrach and R. Maier, *Siberian snake for the cooler synchrotron COSY*, in PACS2001. Proceedings of the 2001 Particle Accelerator Conference (Cat. No.01CH37268), vol. 4, June 2001, pp. 2566–2568 vol.4.
- [23] A. Nass, *Commissioning of the RF Wien filter for a first deuteron EDM measurement at COSY / Jülich*, PoS, SPIN2018 (2018), p. 090.
- [24] *Wasa at Cosy Collaboration*. <http://collaborations.fz-juelich.de/ikp/wasa/>, 2020.
- [25] F. Müller, *Polarimeter Development for Electric Dipole Moment Measurements in Storage Rings*, PhD thesis, RWTH Aachen University, 2019.
- [26] O. Javakhishvili *et al.*, *Development of a multi-channel power supply for silicon photo-multipliers used with inorganic scintillators*, 2020.

-
- [27] R. Brun and F. Rademakers, *ROOT — An object oriented data analysis framework*, Nuclear Instruments and Methods in Physics Research Section A: Accelerators, Spectrometers, Detectors and Associated Equipment, 389 (1997), pp. 81 – 86. New Computing Techniques in Physics Research V.
- [28] F. Müller *et al.*, *Measurement of deuteron carbon vector analyzing powers in the kinetic energy range 170-380 MeV*, (2020).
- [29] G. G. Ohlsen and P. Keaton, *Techniques for measurement of spin-12 and spin-1 polarization analyzing tensors*, Nuclear Instruments and Methods, 109 (1973), pp. 41 – 59.
- [30] J. Pretz and F. Müller, *Extraction of azimuthal asymmetries using optimal observables*, The European Physical Journal C, 79 (2019).
- [31] M. Rosenthal, *Experimental Benchmarking of Spin Tracking Algorithms for Electric Dipole Moment Searches at the Cooler Synchrotron COSY*, PhD thesis, RWTH Aachen University, 2016.
- [32] D. Eversmann, *High Precision Spin Tune Determination at the Cooler Synchrotron in Jülich*, PhD thesis, RWTH Aachen University, 2017.
- [33] *atan2*. <http://en.cppreference.com/mwiki/index.php?title=cpp/numeric/math/atan2&oldid=79630>. Online, accessed March 24, 2020.
- [34] D. Eversmann, J. Pretz, and M. Rosenthal, *Amplitude estimation of a sine function based on confidence intervals and Bayes' theorem*, Journal of Instrumentation, 11 (2016), p. P05003–P05003.
- [35] S. W. Smith, *The Scientist and Engineer's Guide to Digital Signal Processing*, California Technical Publishing, 1997. Available at www.dspguide.com.
- [36] D. E. et al., *New Method for a Continuous Determination of the Spin Tune in Storage Rings and Implications for Precision Experiments*, Phys. Rev. Lett., 115 (2015), p. 094801.
- [37] A. C. Müller and S. Guido, *Introduction to Machine Learning with Python*, 2006.
- [38] F. Chollet *et al.*, *Keras*. <https://keras.io>, 2015.
- [39] M. Abadi *et al.*, *TensorFlow: Large-Scale Machine Learning on Heterogeneous Systems*, 2015. Software available from <https://www.tensorflow.org/>.

-
- [40] A. Zell, *Simulation Neuronaler Netze [Simulation of Neural Networks]*, 1994.
- [41] X. Glorot, A. Bordes, and Y. Bengio, *Deep Sparse Rectifier Neural Networks.*, in AISTATS, vol. 15 of JMLR Proceedings, JMLR.org, 2011, pp. 315–323.
- [42] C. M. Bishop, *Pattern Recognition and Machine Learning (Information Science and Statistics)*, Springer-Verlag, Berlin, Heidelberg, 2006.
- [43] Wikimedia Commons user Glosser.ca, *Artificial neural network with layer coloring.* https://commons.wikimedia.org/wiki/File:Colored_neural_network.svg, 2013. Online, accessed March 14, 2020.
- [44] K. Fukushima and S. Miyake, *Neocognitron: A new algorithm for pattern recognition tolerant of deformations and shifts in position*, Pattern Recognition, 15 (1982), pp. 455–469.
- [45] StackExchange user Vinzza, *Example of a convolutional layer operation.* <https://tex.stackexchange.com/questions/437007/drawing-a-convolution-with-tikz>, 2018. Online, accessed April 6, 2020.
- [46] J. (juyang Weng, N. Ahuja, and T. S. Huang, *Cresceptron: a self-organizing neural network which grows adaptively*, in In Proc. Int’l Joint Conference on Neural Networks, 1992, pp. 576–581.
- [47] Computer Science Wiki User FireLordPhoenix, *Pictorial example of max-pooling*, 2018. Online, accessed March 15, 2020.
- [48] S. Saha, *A Convolutional Neural Network sequence to classify handwritten digits.* <https://towardsdatascience.com/a-comprehensive-guide-to-convolutional-neural-networks-the-eli5-way-3bd2b1164a53>, 2018. Online, accessed March 24, 2020.
- [49] R. Y. Rubinstein and D. P. Kroese, *The Cross Entropy Method: A Unified Approach To Combinatorial Optimization, Monte-Carlo Simulation (Information Science and Statistics)*, Springer-Verlag, Berlin, Heidelberg, 2004.
- [50] I. Goodfellow, Y. Bengio, and A. Courville, *Deep Learning*, MIT Press, 2016. <http://www.deeplearningbook.org>.
- [51] D. Kingma and J. Ba, *Adam: A Method for Stochastic Optimization*, 2014.

- [52] J. Pretz, *Comparison of methods to extract an asymmetry parameter from data*, Nuclear Instruments and Methods in Physics Research Section A: Accelerators, Spectrometers, Detectors and Associated Equipment, 659 (2011), p. 456–461.

List of Figures

2.1. EDM and CP Violation.	4
2.2. Vertical polarisation build due to an EDM.	7
3.1. Schematic of COSY.	10
3.2. Interior of the RF Wien Filter.	12
3.3. Schematic of WASA.	14
3.4. JePo Polarimeter.	14
4.1. Measurement principle.	16
4.2. Coordinate System.	17
4.3. Integrated Count Rates as a function of turn numbers in COSY.	18
4.4. Vertical Polarisation ϵ_V	20
4.5. Fake EDM signals.	20
4.6. Basic principle of the mapping method.	22
4.7. Spin Phase Advance in the up and down detector for two different fixed spin tunes.	23
4.8. Vertical Asymmetry.	24
4.9. Horizontal polarisation, calculated with the mapping method.	25
4.10. Basic principle of the Fourier method.	27
4.11. Fourier Coefficients a_{ν_k} and b_{ν_k}	29
4.12. Fourier Amplitudes.	30
4.13. Phase Shift Explanation.	32
4.14. Effects of the phase for different fixed spin tunes.	33
4.15. Comparison of the horizontal polarisation, determined with different methods.	35
4.16. Comparison of the phase φ_s , calculated with different methods.	36
4.17. Comparison of the spin tune, calculated with different methods.	36
4.18. Amplitudes measured by the individual detectors with data from an unpolarized cycle.	38
4.19. Visualisation of the new online luminosity monitoring tool.	40
4.20. Horizontal polarisation ϵ_H , phase φ_s and spin tune ν_s as a function of turn numbers for Run 50291 Cycle 2.	43
4.21. a and ϵ_H for a run where the phase feedback was turned on.	44
4.22. Combined Spin Tunes.	44
4.23. Results of run 50289 cycle 1.	45

4.24. Peaks determined with different methods.	47
4.25. Weighted Spin Tune from run 50370 cycle 5.	48
4.26. Horizontal polarisation ϵ_H , phase φ_s and spin tune ν_s as a function of turn numbers for Run 50122 Cycle 2.	49
4.27. ReLU activation function, used in this work.	51
4.28. A schematic sketch of an artificial neural network.	52
4.29. Principle of convolutional layers.	53
4.30. Schematic principle of Max Pooling Layers.	53
4.31. An example of a full architecture of an neural network.	54
4.32. Training Data.	56
4.33. a) Accuracy and Loss b) Validation Accuracy and Validation Loss, when training on the real data training set	57
4.34. Network Architecture used in this work.	58
4.35. Peaks detected by the neural network in a frequency range from 3.75 Hz to 11 000 Hz.	60
4.36. Peaks detected by the neural network in a frequency range from 115 845 Hz to 125 801.25 Hz.	61
4.37. Peaks detected by the neural network in a frequency range from 465 285 Hz to 472 833.75 Hz.	62

List of Tables

2.1. Rough estimates of particular values of deuterons (d) and protons (p) at a momentum of 970 MeV/ c and 520 MeV/ c in COSY respectively, including the particles revolution frequency f_{rev} , anomalous G factors [12, 13], Lorentz factors β and γ , the spin tune γG and the spin tune in units of hertz $f_{\text{prec}} = \gamma G f_{\text{rev}}$. . .	7
4.1. Root Tree Information.	16
4.2. Results of the least square fits, shown in Figure 4.7a.	22

Acknowledgments

First of all i would like to give my sincere gratitudes to Prof. Dr. Jörg Pretz for giving me the opportunity to write this thesis and introducing me into the fascinating topic of electric dipole moments. His motivation and patience mainly contributed to the success of this thesis and created a pleasant working atmosphere during the last year.

I would like to thank Prof. Dr Achim Stahl for acceding to be the second supervisor of this work.

A big thank you goes to Dr. Volker Hejny for all his advices and patience regarding the analysis. Without him, this thesis would be half as long as it is now.

I would like to thank the staff of IKP for fruitful discussions before, during and after our regular analysis meetings.

I cannot forget to thank my fellow students namely Vera, Tim, Christian, Saad, Abiroop, Maximillian, Benat and Mathis for introducing the cake wednesday, countless numbers of coffee breaks and for suffering together during tedious bus rides to Jülich and Aachen. Also i would like to thank Niklas, Max and Yannic for making the past five years an unforgettable time.

Finally i would like to thank my parents for supporting me during the last years. All i had to worry about was physics. I know this is not self-evident.

Eidesstaatliche Versicherung

Ich versichere hiermit an Eides Statt, dass ich die vorliegende Masterarbeit mit dem Titel *Polarisation Measurements for Storage Ring Electric Dipole Moment Investigations* selbstständig und ohne unzulässige fremde Hilfe erbracht habe. Ich habe keine anderen als die angegebenen Quellen und Hilfsmittel benutzt. Die Arbeit hat in gleicher oder ähnlicher Form noch keiner Prüfungsbehörde vorgelegen.

Aachen, den 04. Mai 2020

Achim Andres